14

Modelling Friction Contacts in Structural Dynamics and its Application to Turbine Bladed Disks

Christian Maria Firrone and Stefano Zucca
Politecnico di Torino, Department of Mechanics,
Italy

1. Introduction

Modelling the effect of friction contacts in structural dynamics (Awrejcewicz & Pyryev, 2009) has become a major issue in the design of machines (Awrejcewicz et al, 2008a) and structures. In order to obtain reliable predictions of the stress levels in vibrating structures, one of the key points is dry friction modelling (Awrejcewicz et al, 2008b).

In the dynamic design of turbine bladed disks (Srinivasan, 1997; Szwedowicz, 2008), friction damping generated at sliding contacts plays a relevant role, since due to the high modal density of these components and to the wide spectrum of the dynamic excitation , the complete detuning of the bladed disk is not often a feasible design option and resonances may occur. In order to prevent high cycle fatigue failures due to large response levels at resonance, friction dampers are commonly designed and added to bladed disks in order to reduce the vibration amplitude.

The commonest sources (Fig. 1) of friction damping in turbine bladed disks are the blade-disk interfaces (Petrov & Ewins, 2005; Charleux et al, 2006; Allara et al., 2007), the shrouds (Yang & Menq, 1998c; Petrov & Ewins, 2003; Siewert et al, 2009) located at the blade tip in order to connect adjacent blades by interference, and underplatform dampers (Csaba, 1998; Yang & Menq, 1998a-b; Sanliturk et al, 2001; Panning et al, 2003; Petrov & Ewins, 2007; Szwedowicz et al., 2008; Zucca et al, 2008; Cigeroglu et al., 2009; Firrone et al., 2011), metal devices located under the blade platforms and pressed against them during rotation by the centrifugal force.

In order to compute the forced response of bladed disks with friction contacts, commercial finite element codes are not suitable since they are based on the time integration method of the non-linear differential balance equations and they require very large calculations times, which make unfeasible any parametric analysis typical of the design phase.

For this reason, ad hoc numerical codes must be developed in order to compute the forced response in the frequency domain. These codes are based on the Harmonic Balance Method (HBM) (Cardona et al. 1998): the periodic variables (displacements and forces) are expressed as a superposition of harmonic terms by Fourier analysis and then the balance of each harmonic is imposed, turning the original nonlinear differential equations in a set of nonlinear algebraic equations.
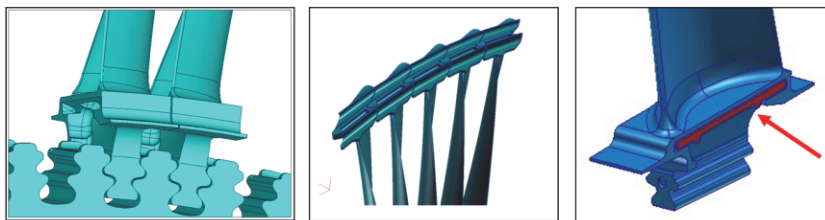
Fig. 1. Different types of friction contacts in turbine bladed disks: blade root joints, blade shrouds and underplatform dampers

In order to couple the bodies in contact when operating in the frequency domain, several contact elements have been developed. The main 4 contact elements available in the literature are:

- 1D tangential relative displacement and constant normal load (Griffin, 1980),
- 1D tangential relative displacement and variable normal load (Yang et al, 1998; Petrov & Ewins, 2003),
- 2D tangential relative displacement and constant normal load (Sanliturk & Ewins, 1996; Menq & Yang, 1998),
- 2D tangential displacement and variable normal load (Yang & Menq, 1998c).

Due to the complex kinematics of friction contacts, contact models A and C, neglecting the variation of normal loads during the system vibration, are not suitable for implementation, since they do not allow modelling partial lift-off during vibration, while the contact models B and D have established themselves as the references to model friction contacts.

All the above mentioned contact models have a common feature: for the periodical contact forces to be computed, the value of a static normal pre-load must be provided, as a result of a preliminary static analysis of the system. In (Firrone et al, 2011), it has been demonstrated that the preliminary static analysis is not necessary and that the simultaneous calculation of static and dynamic contact forces is possible.

In this chapter, the numerical methods currently employed to simulate the forced response of turbine bladed disks with friction interfaces are analyzed; in detail:

- The balance equation of the bodies in contact are deduced in the frequency domain by means of the harmonic balance method.
- The main contact elements available in the literature are described in order to highlight their main features and their effect on the dynamics of the system.
- The effect of an uncoupled solution strategy based on a preliminary static analysis followed by the dynamic analysis are highlighted and the coupled static/dynamic approach for the simultaneous calculation of the contact forces is described in detail, describing also the effect of multiple harmonics.
- The critical issues arising when the methods are applied to full scale applications are discussed, with emphasis on reduction techniques and modelling distributed contacts.
- Case studies, representing typical configurations of friction contacts in turbine bladed disks are presented and the effect of the friction contacts on the forced response curves are computed and discussed.
- The numerical methods necessary to solve the set of non-linear algebraic equations are analyzed and different Continuation strategies are discussed.

2. Balance equations and Harmonic Balance Method (HBM)

The starting point in the forced response calculation of a mechanical system with friction contacts is the development of the finite element (FE) model of the system, whose balance equations are

$$M \cdot \ddot{Q} + C \cdot \dot{Q} + K \cdot Q = F_E + F_{NL}\left(Q, \dot{Q}\right) \tag{1}$$

where M, C and K are the mass, damping and stiffness matrices of the system, Q is the displacement vector of degrees of freedom (dofs), F_E are the periodical external forces acting on the system and F_{NL} are the nonlinear forces, generated at the friction contacts by the relative displacements of the contact nodes.

In order to reduce the calculation times typical of numerical integration of non-linear systems, the harmonic balance method (HBM) can be used to compute the steady-state response of the system (Cardona et al, 1998; Griffin, 1980; Petrov & Ewins 2003).

In detail, due to the periodicity of the external excitation, also the displacements Q and the non-linear forces F_{NL} are periodical at steady-state. Therefore they can be expressed as a truncated series of harmonic terms

$$Q = Q^{(0)} + \Re\left(\sum_{n=1}^{N_H} Q^{(n)} \cdot e^{i \cdot n \cdot \omega \cdot t} \right) \tag{2}$$

$$F_E = F_E^{(0)} + \Re\left(\sum_{n=1}^{N_H} F_E^{(n)} \cdot e^{i \cdot n \cdot \omega \cdot t} \right) \tag{3}$$

$$F_{NL} = F_{NL}^{(0)} + \Re\left(\sum_{n=1}^{N_H} F_{NL}^{(n)} \cdot e^{i \cdot n \cdot \omega \cdot t} \right) \tag{4}$$

where N_H is the maximum number of harmonics and ω is the fundamental frequency of the excitation forces acting on the system. The generic harmonic coefficient $X^{(n)}$ (n>1) is a complex quantity. If Equations (2)-(4) are replaced into the balance equation (1), the following sets of algebraic complex equations are deduced

$$D^{(n)} \cdot Q^{(n)} = F_E^{(n)} + F_{NL}^{(n)} \text{ with n = 0..N}_H \tag{5}$$

where $D^{(n)} = -(n\omega)^2 M + in\omega C + K$ is the nth dynamic stiffness matrix of the system and the 0th order represents the static balance equation.

Since the non-linear contact forces $F_{NL}^{(n)}$ depend on the relative displacement of contact dofs and since the number of contact dofs is typically much lower than the number of total dofs, it is convenient to rearrange equations (5) in order to decouple the solution of the non-linear part of the system from its linear part. To do this, the receptance matrix $R^{(n)}$, inverse of $D^{(n)}$ matrix, can be computed and the set of balance equations can be written in the receptance form

$$Q^{(n)} = Q_E^{(n)} + R^{(n)} \cdot F_{NL}^{(n)} \tag{6}$$

where the first term at the right hand side of equation (6) is the linear response due to the external excitation. i.e. $Q_E^{(n)} = R^{(n)} \cdot F_E^{(n)}$, while the second terms takes into account the contribution of the non-linear forces.

Then, the displacement vector $Q^{(n)}$ can be split in the non-linear dofs $Q_{NL}^{(n)}$ where the nonlinear contact forces act and all the other linear dofs $Q_{LN}^{(n)}$, and the balance equations (6) become

$$\begin{Bmatrix} Q_{NL}^{(n)} \\ Q_{LN}^{(n)} \end{Bmatrix} = \begin{Bmatrix} Q_{E,NL}^{(n)} \\ Q_{E,LN}^{(n)} \end{Bmatrix} + \begin{bmatrix} R_{NL,NL}^{(n)} & R_{NL,LN}^{(n)} \\ R_{LN,NL}^{(n)} & R_{LN,LN}^{(n)} \end{bmatrix} \cdot \begin{Bmatrix} F_{NL}^{(n)} \\ 0 \end{Bmatrix} .$$ (7)

Since the non-linear contact forces $F_{NL}^{(n)}$ only depend on the displacement $Q_{NL}^{(n)}$ of non-linear dofs, only the equation

$$Q_{NL}^{(n)} = Q_{E,NL}^{(n)} + R_{NL,NL}^{(n)} \cdot F_{NL}^{(n)}$$ (8)

is non-linear and must be solved iteratively with a non-linear solver, while the response of the linear dofs $Q_{LN}^{(n)}$ can be computed with the equation

$$Q_{LN}^{(n)} = Q_{E,LN}^{(n)} + R_{LN,NL}^{(n)} \cdot F_{NL}^{(n)}$$ (9)

once the non-linear forces $F_{NL}^{(n)}$ are known. It must be observed that the balance equations (8) are coupled to each other, because the arbitrary harmonic component $F_{NL}^{(n)}$ of the non-linear contact forces depends on all the harmonic components of the displacement of non-linear dofs Q_{NL}. In order to solve the non-linear balance equations (8) a contact model is necessary to compute the harmonic components $F_{NL}^{(n)}$ of the periodical contact forces from a given set of harmonics components $Q_{NL}^{(n)}$ of the nodal displacements of non-linear dofs.

3. Contact elements

In the technical literature, the problem of modeling periodical contact forces at friction contacts for their implementation in numerical solvers for the forced response of mechanical systems with friction contacts has been addressed by several authors, leading to several contact models.

All the models are based on the flow-chart show in Fig. 2 and based on the following steps:
-   For given Fourier coefficients $Q_{NL}^{(n)}$ of the displacement of contact nodes of equation (8), relative displacements $\Delta Q_{NL}^{(n)}$ are computed from the contact kinematics.
-   Inverse Fast Fourier Transform (IFFT) is applied to $\Delta Q_{NL}^{(n)}$ to compute the periodical relative displacements ΔQ_{NL} in the time domain.
-   Constitutive laws of the contact model are used to compute the periodical non-linear contact forces F_{NL}.
-   Fast Fourier Transform is applied to F_{NL} to compute the harmonic components $F_{NL}^{(n)}$ of the periodical contact forces to be used in the balance equations (8).
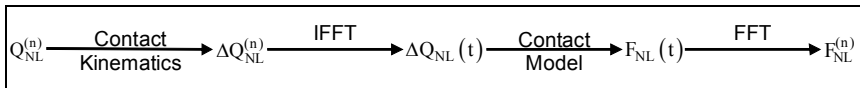

Fig. 2. Typical flow-chart of contact models.

In the literature 4 main contact models exist for the calculation in the frequency domain of the forced response of mechanical systems with friction contacts:

- 1D tangential relative displacement and constant normal load (Griffin, 1980),
- 1D tangential relative displacement and variable normal load (Yang et al, 1998; Petrov & Ewins, 2003),
- 2D tangential relative displacement and constant normal load (Sanliturk & Ewins, 1996; Menq & Yang, 1998),
- 2D tangential displacement and variable normal load (Yang & Menq, 1998c).

In this section the above listed contact models are described and used to simulate the forced response calculation of a single dof system in order to highlight their effect on the system dynamics and to compare their features and their performance.

3.1 1D tangential relative displacement and constant normal load

This contact model (Fig. 3) has been described and used for the first time in (Griffin, 1980). It is able to model 1D relative displacement in the tangential direction and to take into account the effect of a constant normal load acting on the contact.
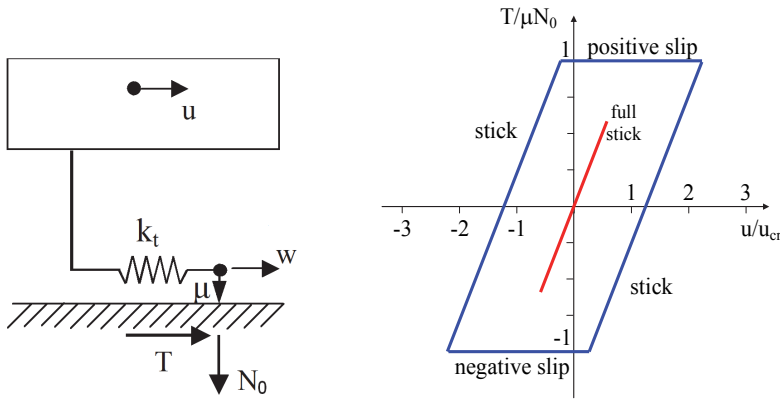

Fig. 3. 1D relative displacements and constant normal load: contact model (left) and typical hysteresis cycles (right)

The tangential contact stiffness is modelled by a spring of stiffness k_t, a coefficient of friction μ is assumed between the contact surfaces while constant static normal load N_0 keeps the bodies in contact. For a given periodic relative displacement of contact nodes $u(t)$ the periodic tangential force $T(t)$ is computed. The amount of tangential slip between the contact surfaces is $w(t)$. Two contact states can be modelled: stick and slip. In the sticking mode, the contact is elastic, no slip occurs, and the tangential force is

$$T = k_t \cdot (u - w) \ \ with \ \ \dot{w} = 0 \,. \tag{10}$$

In the slipping mode, the modulus of the tangential force is equal to the Coulomb limit value and its versus depends on the versus of the slipping velocity according to the equation

$$T = \mathrm{sgn}(\dot{w}) \cdot \mu \cdot N_0 \,, \tag{11}$$

where sgn(x) is the sign function whose values are

$$\text{sgn}(\dot{w}) = \begin{cases} -1 & if \quad \dot{w} < 0 \quad (negative\ slip) \\ 1 & if \quad \dot{w} > 0 \quad (positive\ slip) \end{cases} \tag{12}$$

Stick and slip alternate each other according to the transition criteria shown in Table 1

Contact state	Transition criteria
Stick-to-slip	$|T| = \mu \cdot N_0$
Slip-to-stick	$\dot{w} = 0$

Table 1. 1D contact with constant normal load: transition criteria.

If the amplitude of the tangential relative displacement u(t) is lower than the critical value $u_{cr} = \mu \cdot N_0 / k_t$ the contact is in full stick conditions (red line in Fig. 3) and vibration energy is not dissipated by friction. If the critical value u_{cr} is exceeded alternating stick and slip occur (blue line in Fig. 3) and the area of the hysteresis cycle is the energy dissipated per cycle.
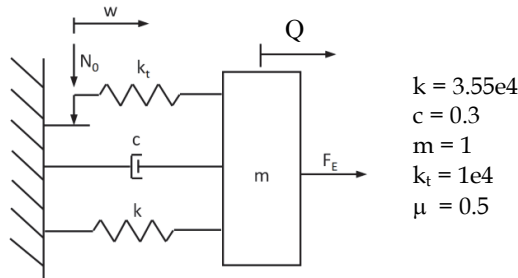

Fig. 4. Single dof description

In order to demonstrate the effect of this contact element on the dynamics of a vibrating system, a single dof system (Fig. 4) is here analyzed. The vibrating system is in contact with a fixed wall and therefore, due to the simple contact kinematics, the relative displacement u(t) in the tangential direction is equal to the absolute displacement Q(t) of the mass.
The forced response is computed for different values of the static normal load N_0 (Fig. 5 – left) and of external excitation F_E (Fig. 5 – right) in order to show the effect of friction contacts on a vibrating structure, using only the first order of the Fourier series.
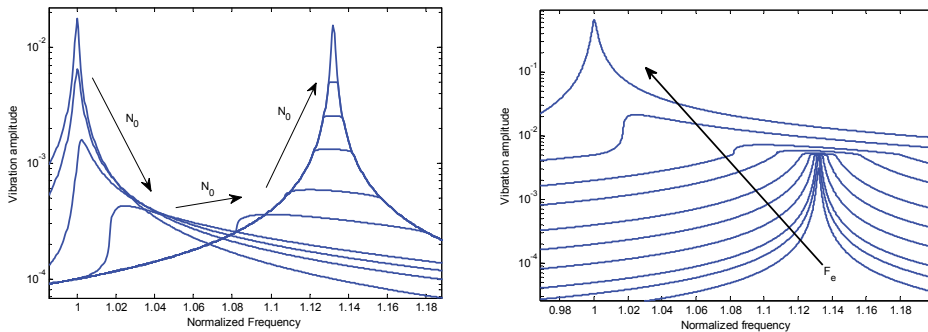

Fig. 5. Effect of N_0 (left) and of F_E (right) on the dynamics of the system

In the first case, at $N_0 = 0$ the response of the linear system is computed since the tangential force T is null. As N_0 growing larger, the maximum response of the system decreases, reaches a minimum value and then increases again as the contact tends towards the full sticking mode. The contact affects not only the damping of the system but also its stiffness since the resonance frequency of the system becomes larger as N_0 increases.

The effect of the external excitation is the opposite. For small values of F_E the contact is in the full sticking mode, while as the excitation force becomes larger, the system tends towards the linear condition.

The effect of N_0 and F_E on the system dynamics can be shown by means of two compact diagrams (Fig. 6) called the optimization and the performance plot, respectively. The optimization plot (Yang & Menq, 1998a, Yang & Menq 1998b) can be used to identify the optimum value of N_0 corresponding to the minimum vibration amplitude of the system.
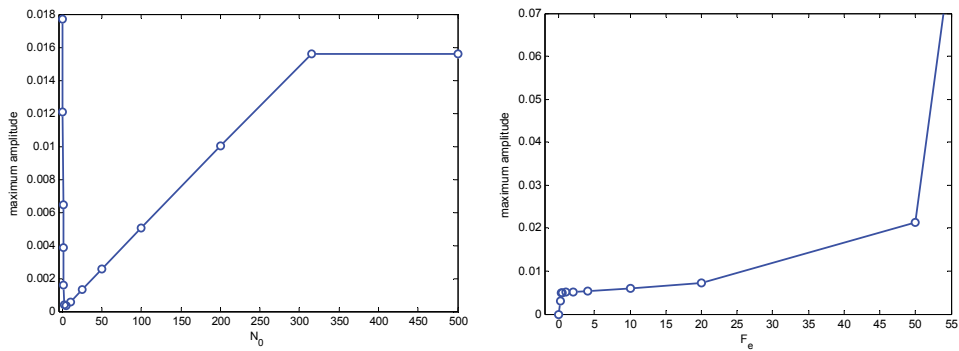

Fig. 6. Optimization and performance plots.

On the contrary, the performance plot can be used to identify the range of external excitation for a robust friction contact design, corresponding to the flat part of the performance curve, where large variations of the external force produce small variations of the system response.

3.2 1D tangential relative displacement and variable normal load.

The contact model described in Section 3.1 is not able to model the effect of the variation of the contact normal load, due to a periodical normal relative displacements of contact points, on the hysteresis cycle and on the energy dissipated by friction.

This important feature can be taken into account by means of the contact model originally developed in (Yang et al., 1998) for the single HBM and then extended in (Petrov & Ewins, 2003) for the multi-harmonic balance method (MHBM).

According to this model, shown in Fig. 7, the tangential and normal contact stiffness are modeled by springs of stiffness k_t and k_n, respectively, a coefficient of friction μ is assumed between the contact surfaces.

The relative displacements in the tangential and normal directions are u(t) and v(t) respectively, while the amount of tangential slip between the contact surfaces is w(t).

The normal contact force N(t) is defined as

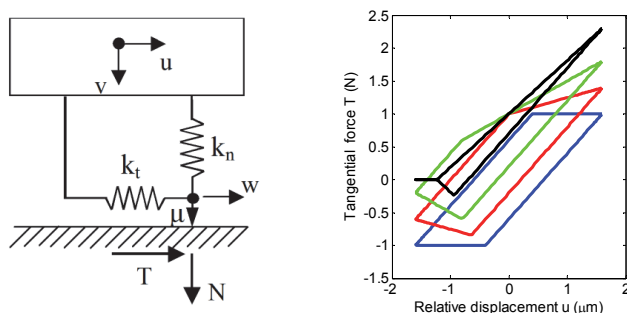$$N = \max\left(N_0 + k_n \cdot v, 0\right) \tag{13}$$

Fig. 7. 1D relative displacements and variable normal load: contact model (left) and typical hysteresis cycles (right)

where N_0 is the static normal load. If N_0 is positive, the bodies are in contact before vibration starts, while if N_0 is negative an initial gap exists between the two bodies. According to the value of the normal relative displacement $v(t)$ three conditions are possible: full contact, partial lift-off and full-lift off. According to equation (13), when lift-off occurs, the normal contact load is set equal to 0, since negative values are not acceptable.

$$T = \begin{cases} k_t \cdot (u\text{-}w) & \text{sticking mode} \\ \text{sgn}(\dot{w}) \cdot \mu \cdot N & \text{slipping mode} \\ 0 & \text{lift-off mode} \end{cases} \quad (14)$$

stick, slip and lift-off (see Equation (14) for the constitutive equations) may alternate each other during the periodic vibration, according to the transition criteria shown in Table 2.

Initial state	Final state	Criteria
Stick	Slip	$|T| = \mu \cdot N$
	Lift-off	$N = 0 \ and \ \dot{N} < 0$
Slip	Stick	$\dot{w} = 0$
	Lift-off	$N = 0 \ and \ \dot{N} < 0$
Lift-off	Stick	$N = 0 \ and \ \dot{N} > 0 \ \text{and} \ |\dot{T}| < \mu \cdot \dot{N}$
	Slip	$N = 0 \ and \ \dot{N} > 0 \ \text{and} \ |\dot{T}| > \mu \cdot \dot{N}$

Table 2. 1D contact with variable normal load: transition criteria.

The effect of the variable normal contact load $N(t)$ on the hysteresis cycle of the tangential contact load $T(t)$ is shown in Fig. 7, where a sinusoidal $v(t)$ is in-phase with a sinusoidal $u(t)$. If $v(t)$ is null, the contact model is coincident with the model of Section 3.1 (blue line). As the amplitude of $v(t)$ growing larger, the shape and the area of the cycle change. In case of full contact (blue, red and green lines) the alternating stick-slip phenomenon occurs, but when the value of $v(t)$ becomes so large that partial lift-off occurs (black line), then a horizontal segment at $T(t)=0$ appears, and the cycle becomes a triangle.

Fig. 8 shows the effect of the variable normal contact load on the dynamic behavior of the vibrating structures.
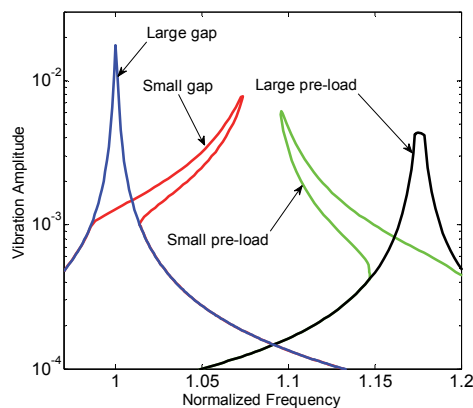
Fig. 8. Effect of N_0 on the dynamics of the system with variable normal contact load.

The blue line refers to such a large gap ($N_0 \ll 0$) that no contact occurs during the vibration and the system response corresponds to the response of the free system without contact. The red line, partly overlapping the blue line, represents a case of small gap ($N_0 < 0$) which is closed during vibration due to the normal relative displacements of the contact points. The stiffening effect of the closing contact on the resonance peak is clearly visible, as well as the existence of multiple solutions for a certain range of vibration frequencies. At the same way, the green curve refers to a positive pre-load ($N_0 > 0$), not large enough to prevent lift-off during vibration. In this case, the softening effect of the opening contact on the resonance peak is visible. Finally, the black curve represents a case of a large pre-load ($N_0 \gg 0$), which imposes full contact conditions during the periodic vibration.

3.3 2D tangential relative displacement and constant normal load.

The contact models described in Sections 3.1 and 3.2 are able to simulate the behavior of friction contact in case of 1D tangential relative displacements. However, in several applications, 2D tangential relative displacements of the contact points occur and modeling these contact assuming a linear trajectory can lead to an underestimation of the friction damping (Griffin & Menq, 1991). In order to model this feature, two different modeling techniques are available:

1. to use two 1D contact elements like those described in Sections 3.1 and 3.2, placed orthogonal to each other, in order to take into account the 2D trajectory of the contact points on the contact plane;
2. to use a 2D contact element able to take into account the coupling between the two orthogonal components of the tangential relative displacements.

The second approach is possible using a contact model developed independently in (Sanliturk & Ewins, 1996) and (Menq & Yang, 1998) characterized by 2D tangential relative displacement and constant normal load (Fig.9, left).

Being (x,y) the contact plane, the tangential contact stiffness is modeled by two springs of stiffness k_{tx} and k_{ty} along the two orthogonal directions, a coefficient of friction μ is assumed between the contact surfaces while constant static normal load N_0 keeps the bodies in contact.

For a given periodic relative displacement of contact nodes $u(t) = \{u_x(t); u_y(t)\}$ the periodic tangential force $T(t) = \{T_x(t); T_y(t)\}$ is computed. The amount of tangential slip between the contact surfaces is $w(t) = \{w_x(t); w_y(t)\}$.

Two contact states can be modeled: stick and slip. In the sticking mode, the contact is elastic, no slip occurs, and the tangential force is

$$\begin{Bmatrix} T_x \\ T_y \end{Bmatrix} = \begin{bmatrix} k_{tx} & 0 \\ 0 & k_{ty} \end{bmatrix} \cdot \left(\begin{Bmatrix} u_x \\ u_y \end{Bmatrix} - \begin{Bmatrix} w_x \\ w_y \end{Bmatrix} \right) with \begin{Bmatrix} w_x \\ w_y \end{Bmatrix} = \begin{Bmatrix} 0 \\ 0 \end{Bmatrix} \tag{15}$$

In the slipping mode, the modulus of the tangential force is equal to the Coulomb limit value

$$\sqrt{T_x^2 + T_y^2} = \mu \cdot N_0 \tag{16}$$

On the contact plane, Equation (16) represents the equation of a circumference of radius equal to $\mu \cdot N_0$. In slipping conditions, the friction contact force is oriented along the circumference radius (see Fig.9, right). Stick and slip may alternate each other according to the transition criteria fully described in (Sanliturk & Ewins, 1996; Menq & Yang, 1998). In Fig. 9 (right), different trajectories of the tangential contact force are shown over the contact plane. All the curves refer to sinusoidal relative displacements $u_x = u_{x0} \sin(2\pi t)$ and $u_y = u_{y0} \sin(2\pi t + \phi)$, with $u_{x0}/u_{y0} = 2.5$ and $\phi = \pi/2$. The red curves refer to cases where the contact is in full sticking conditions and no slip occurs between the contact points. The blue curves, on the contrary represent three cases where the vibration amplitude is large enough to induce alternating stick-slip phenomena. In detail, the slipping parts of the cyclic force are those where the blue lines are overlapped over the black circle which represents the Coulomb limit which cannot be exceeded by the tangential force $T(t)$.

If the vibration amplitude increases further, the blue line will overlap completely the black circle, having a full slip condition, which cannot occur in case of 1D tangential relative displacement.
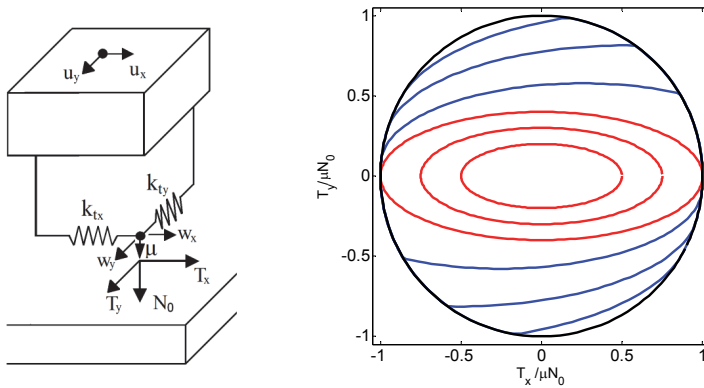

Fig. 9. 2D relative displacements and constant normal load: typical trajectories of the tangential contact forces.

In order to show the effect of the 2D contact kinematics on the behaviour of vibrating structures, a simple dynamic system is here analyzed. A mass vibrates over an (x,y) plane.

Q_x and Q_y are the modal displacement components, they are harmonic quantities $Q_x = Q_{x0}$ $\sin(\omega t)$ and $Q_y = Q_{y0} \sin(\omega t + \pi/2)$, the ratio $Q_{x0}/Q_{y0} = 1$, so that a circular motion of the system is obtained.
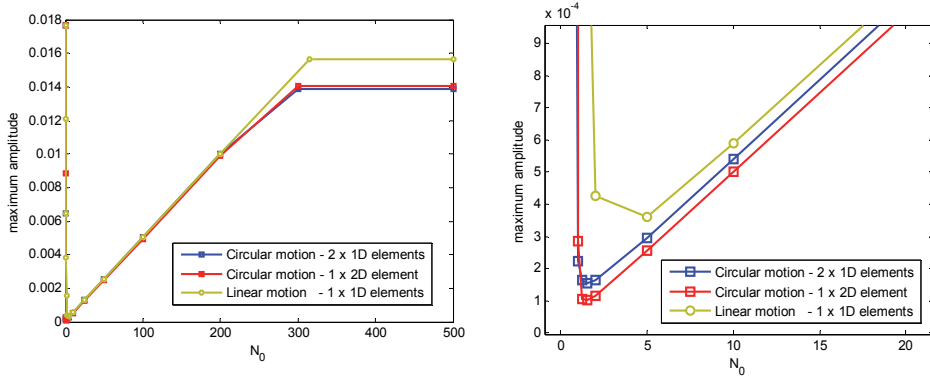

Fig. 10. Optimization curves: full view (left) and zoom around the optimum value (right)

The system dynamics is analyzed for different values of the normal pre-load N_0 and the resulting optimization curves are computed. The contact is modeled in three different ways. In the first way, the y-component of the trajectory is neglected and the contact is modeled with a 1D contact element oriented along the x direction. In the second case, two 1D contact elements (see Section 3.1) are oriented along the x and y directions respectively, while in the third case one 2D contact element described in the current section is used. The optimization curves of the friction contact are shown in Fig. 10.

If the trajectory of the contact point is modeled as linear (1st case) neglecting the y component, the friction damping is not correctly predicted (Griffin & Menq, 1991) and the minimum vibration amplitude is overestimated with respect to the 2nd and the 3rd case. The comparison between the 2nd and the 3rd case does not show significant differences, indicating that both the uncoupled approach based on two orthogonal 1D contact elements and the coupled approach based on one 2D contact element catch the fundamental features of the bi-dimensional trajectory of the contact point.

3.4 2D tangential displacement and variable normal load.

The most advanced contact model available in the literature, consider both the 2D trajectory of the contact points on the contact plane and the periodical variation of the normal load (Yang & Menq, 1998c), see Fig.11, left.

Being (x,y) the contact plane, the tangential contact stiffness is modeled by two springs of stiffness k_{tx} and k_{ty} along the two orthogonal directions, a coefficient of friction μ is assumed between the contact surfaces while variable static normal load defined as

$$N = \max\left(N_0 + k_n \cdot v, 0\right) \tag{17}$$

keeps the bodies in contact.

For a given periodic relative displacement of contact nodes $u(t) = \{u_x(t); u_y(t)\}$ the periodic tangential force $T(t) = \{T_x(t); T_y(t)\}$ is computed. The amount of tangential slip between the contact surfaces is $w(t) = \{w_x(t); w_y(t)\}$.

Three contact states can be modeled: stick, slip and separation. In the sticking mode, the contact is elastic, no slip occurs, and the tangential force is

$$\begin{Bmatrix} T_x \\ T_y \end{Bmatrix} = \begin{bmatrix} k_{tx} & 0 \\ 0 & k_{ty} \end{bmatrix} \cdot \left(\begin{Bmatrix} u_x \\ u_y \end{Bmatrix} - \begin{Bmatrix} w_x \\ w_y \end{Bmatrix} \right) with \begin{Bmatrix} w_x \\ w_y \end{Bmatrix} = \begin{Bmatrix} 0 \\ 0 \end{Bmatrix} \text{ and N} \geq 0. \tag{18}$$

In the slipping mode, the modulus of the tangential force is equal to the Coulomb limit value and its directed parallel to the slip velocity $\dot{w}$.

$$\begin{Bmatrix} T_x \\ T_y \end{Bmatrix} = \mu N \Big/ \|\dot{w}\| \cdot \begin{Bmatrix} \dot{w}_x \\ \dot{w}_y \end{Bmatrix} \quad \text{with } \|\dot{w}\| = \sqrt{\dot{w}_x^2 + \dot{w}_y^2} \tag{19}$$

When separation of the contact points occurs, both the normal and the tangential contact forces are equal to zero. Transitions between contact states are governed by transition criteria described in (Yang & Menq, 1998c).

Four examples of contact force trajectories over the contact plane are shown in Fig. 11, where the blue lines represent the contact force and the black line the Coulomb limit curve. In detail, they represent:

a. A case with constant normal load $N=N_0$, which could be also simulated with the contact model described in Section 3.3
b. A case with a small variation of N, with clearly visible alternating stick-slip states
c. A case with a large variation of N, with suppression of one of the stick states
d. A case with a very large variation of N, inducing partial separation of the contact points, corresponding to the point where the trajectory passes through the origin.
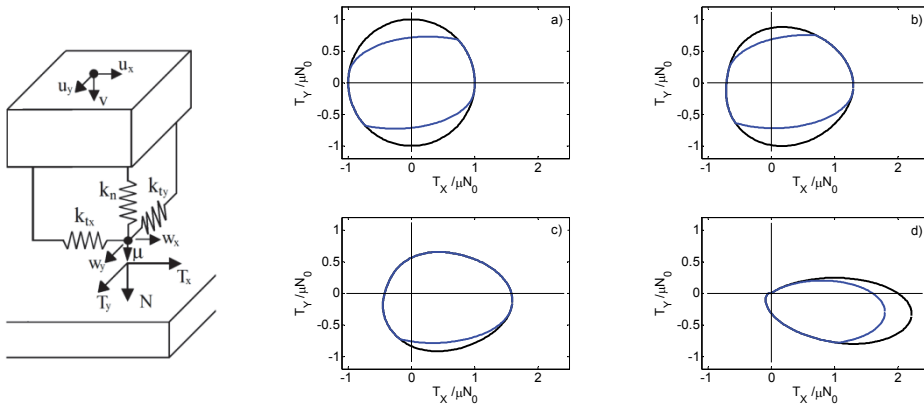
Fig. 11. Tangential contact force trajectories on the contact plane

4. Static/dynamic coupling and higher order harmonics

The contact models introduced in Section 3 share a common feature, i.e., they all need a normal load N_0 as an input parameter together with the variable relative displacements u(t) and v(t) in order to calculate the hysteresis loop of the tangential force T(t). It is easy to understand that an accurate calculation of N_0 is of primary importance when those contact

models are applied to practical problems to calculate the forced response of structures with friction joints, since N_0 determines the amount of stick and slip of the contact, therefore the amount of friction damping. The value of N_0 cannot be chosen in an arbitrary way, since it represents the static normal pre-load acting on the friction contact. The commonest strategy is to use the pre-loads obtained by the solution of the static equilibrium of the structure, assuming that the oscillating response is superimposed to the static deformed shape. In fact, the static equilibrium can take into account the influence of the weight of the bodies in contact or the interference and the presence of the centrifugal force for rotating components. In order to address the issue of the choice of N_0 over the contact and its consequence on the calculation of the forced response of the structure, the simple structure shown in Fig. 12 is modelled and the differential equilibrium equations of the system are integrated in the time domain (DTI, Direct Time Integration). The 2D structure of Figure 12 is a simplified representation of two blades of a blade array of a turbine rotor and a blade-to-blade friction damper (the so called underplatform damper, see introduction and Fig. 1), i.e., a metal component pressed against the blades platforms during rotation by the centrifugal force. Each blade is modelled with two masses (m_1 the platform and m_2 the blade airfoil) and has three dofs (q_{x1}, q_{x2}, q_y). The underplatform damper is modelled as a rigid body with 3 dofs, whose center of mass is connected to ground by a set of linear springs and viscous dampers. Moreover, the underplatform damper has a triangular shape and the contact with the two platforms is modeled with a node-to-node contact element allowing for a 1D relative displacement and a variable normal load (contact model B, Section 3.2, see Fig. 7). The positive axis for the tangential relative displacement u for both the contact elements is oriented toward the apex of the underplatform damper (Fig. 12b) while, accordingly to Fig. 7, v is positive during contact. The system has nine dofs and the values of the structural parameters are listed below the Fig. 12. The centrifugal load CF is applied to the center of mass of the underplatform damper while two symmetrical harmonic horizontal forces $F_x(t)$ act on the blades.

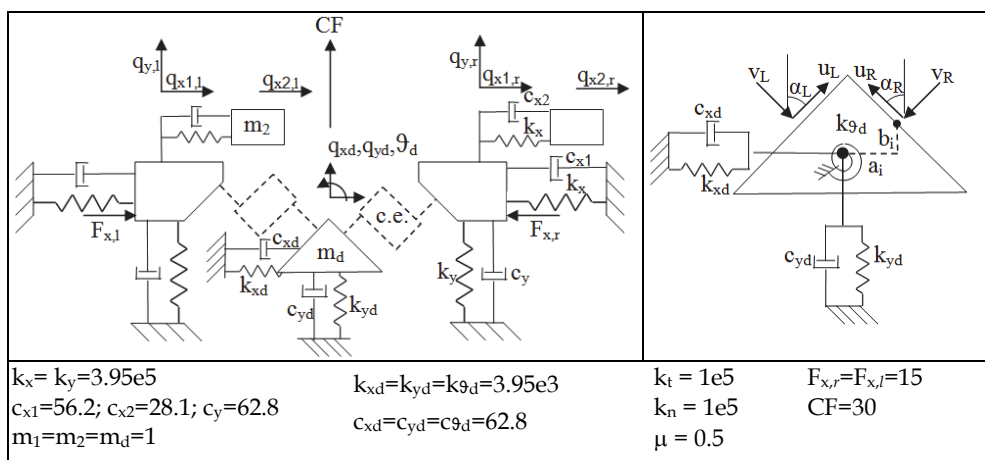| $k_x= k_y=3.95e5$			
$c_{x1}=56.2$; $c_{x2}=28.1$; $c_y=62.8$	$k_{xd}=k_{yd}=k\vartheta_d=3.95e3$	$k_t = 1e5$	$F_{x,r}=F_{x,l}=15$
$m_1=m_2=m_d=1$	$c_{xd}=c_{yd}=c\vartheta_d=62.8$	$k_n = 1e5$	CF=30
		$\mu = 0.5$	

Fig. 12. Multiple dof description, blade-to-blade friction damper application

4.1 Integration of the balance equations in the time domain

The second order differential equilibrium equations of the nine degrees of freedom of the system of Figure 12 are:

$$m_1 \ddot{q}_{x1,l} + c_{x1}\dot{q}_{x1,l} + k_{x1}q_{x1,l} + c_{x2}\left(\dot{q}_{x2,l} - \dot{q}_{x1,l}\right) + k_{x2}\left(q_{x2,l} - q_{x1,l}\right) = F_{x,l} - F_{Cx,l}$$

$$m_1 \ddot{q}_{y,l} + c_y\dot{q}_{y,l} + k_y q_{y,l} = -F_{Cy,l}$$

$$m_2 \ddot{q}_{x2,l} - c_{x2}\left(\dot{q}_{x2,l} - \dot{q}_{x1,l}\right) - k_{x2}\left(q_{x2,l} - q_{x1,l}\right) = 0$$

$$m_1 \ddot{q}_{x1,r} + c_{x1}\dot{q}_{x1,r} + k_{x1}q_{x1,r} + c_{x2}\left(\dot{q}_{x2,r} - \dot{q}_{x1,r}\right) + k_{x2}\left(q_{x2,r} - q_{x1,r}\right) = F_{x,r} - F_{Cx,r}$$

$$m_1 \ddot{q}_{y,r} + c_y\dot{q}_{y,r} + k_y q_{y,r} = -F_{Cy,r} \qquad (20)$$

$$m_2 \ddot{q}_{x2,r} - c_{x2}\left(\dot{q}_{x2,r} - \dot{q}_{x1,r}\right) - k_{x2}\left(q_{x2,r} - q_{x1,r}\right) = 0$$

$$m_d \ddot{q}_{xd} + c_{xd}\dot{q}_{xd} + k_{xd}q_{xd} = F_{Cx,l} + F_{Cx,r}$$

$$m_d \ddot{q}_{yd} + c_{yd}\dot{q}_{yd} + k_{yd}q_{yd} = F_{Cy,l} + F_{Cy,r} + CF$$

$$I_d \ddot{\vartheta}_d + c_{\vartheta d}\dot{\vartheta}_d + k_{\vartheta d}\vartheta_d = -F_{Cx,l}b_l + F_{Cy,l}a_l - F_{Cx,r}b_r + F_{Cy,r}a_l$$

where $F_{Cx,l}$, $F_{Cy,l}$, $F_{Cx,r}$, $F_{Cy,r}$ are the contact forces acting on the damper projected over the horizontal and vertical direction respectively for the left and right side. If α_L and α_R are the left and right angle between the left and right inclined platform and the vertical axis, it is:

$$F_{Cx,l} = T_l \sin(\alpha_L) + N_l \cos(\alpha_L); \quad F_{Cy,l} = T_l \cos(\alpha_L) - N_l \sin(\alpha_L)$$

$$F_{Cx,r} = -T_r \sin(\alpha_R) - N_r \cos(\alpha_R); \quad F_{Cy,r} = T_r \cos(\alpha_R) - N_r \sin(\alpha_R) \qquad (21)$$

Equilibrium equations (20) are rewritten in terms of a first order differential problem and are solved using the explicit Runge-Kutta formula, Dormand-Prince pair (ODE45) in MATLAB code. The external loads (centrifugal force and blade excitations) are applied according to two load-steps shown in Fig. 13a and Fig. 13b: first a quasi-static application of the centrifugal force determines the static deformation of the system and the static contact loads over the contacts. During this load step the forces on the blades are set to zero ($F_{x,l} = F_{x,r} = 0$). Second, once the static equilibrium of the system is achieved, the harmonic excitations on the two blades $F_{x,l}$ and $F_{x,r}$ are applied by linearly increasing their amplitude (Fig. 13b). The last set of displacements of the first load step is used as first set for the second load step, while the centrifugal force CF is kept constant to 30 N. The excitation frequency is equal to the first natural frequency of the blade (61.8 Hz). The contact forces are calculated once the relative displacements at the two contacts are calculated from the absolute displacements of the system:

$$u_L = (q_{x1,l} - q_{xd,l})\cdot\sin\alpha_L + (q_{y,l} - q_{yd,l})\cdot\cos\alpha_L; \quad u_R = -(q_{x1,r} - q_{xd,r})\cdot\sin\alpha_R + (q_{y,r} - q_{yd,r})\cdot\cos\alpha_R$$

$$v_L = (q_{x1,l} - q_{xd,l})\cdot\cos\alpha_L - (q_{y,l} - q_{yd,l})\cdot\sin\alpha_L; \quad v_R = -(q_{x1,r} - q_{xd,r})\cdot\cos\alpha_R - (q_{y,r} - q_{yd,r})\cdot\sin\alpha_R \qquad (22)$$

where $q_{xd,l}$, $q_{yd,l}$, $q_{xd,r}$, $q_{yd,r}$ are the local absolute displacement of the damper at the left and right side respectively:

$$\begin{Bmatrix} q_{xd,i} \\ q_{yd,i} \end{Bmatrix} = \begin{bmatrix} 1 & 0 & -b_i \\ 0 & 1 & a_i \end{bmatrix} \cdot \begin{Bmatrix} q_{x,d} \\ q_{y,d} \\ \vartheta_d \end{Bmatrix} \quad i = l,r \qquad (23)$$

being a_i and b_i the horizontal and vertical coordinates of the two contact points from the center of mass of the damper. Then the system reacts under the effect of the external loads and of the contact forces whose transitions are calculated according to the criteria in Table 2.

Since the structure is symmetric and the loads are applied symmetrically, also the response of the two blades is symmetric, therefore only the results referred to the left blade are shown. Fig. 13c and Fig. 13d show the tip displacement of the blade (mass m_2) respectively for the first and second load step. It can be noted that in the first load step, as expected, the left blade is pushed toward negative values of the x-axis (symmetrically, the right blade is pushed toward the positive x-axis of the same amount). The tangential contact force T acting on the left side of the damper is displayed in Fig. 13e-f together with the boundaries $\pm\mu N$.

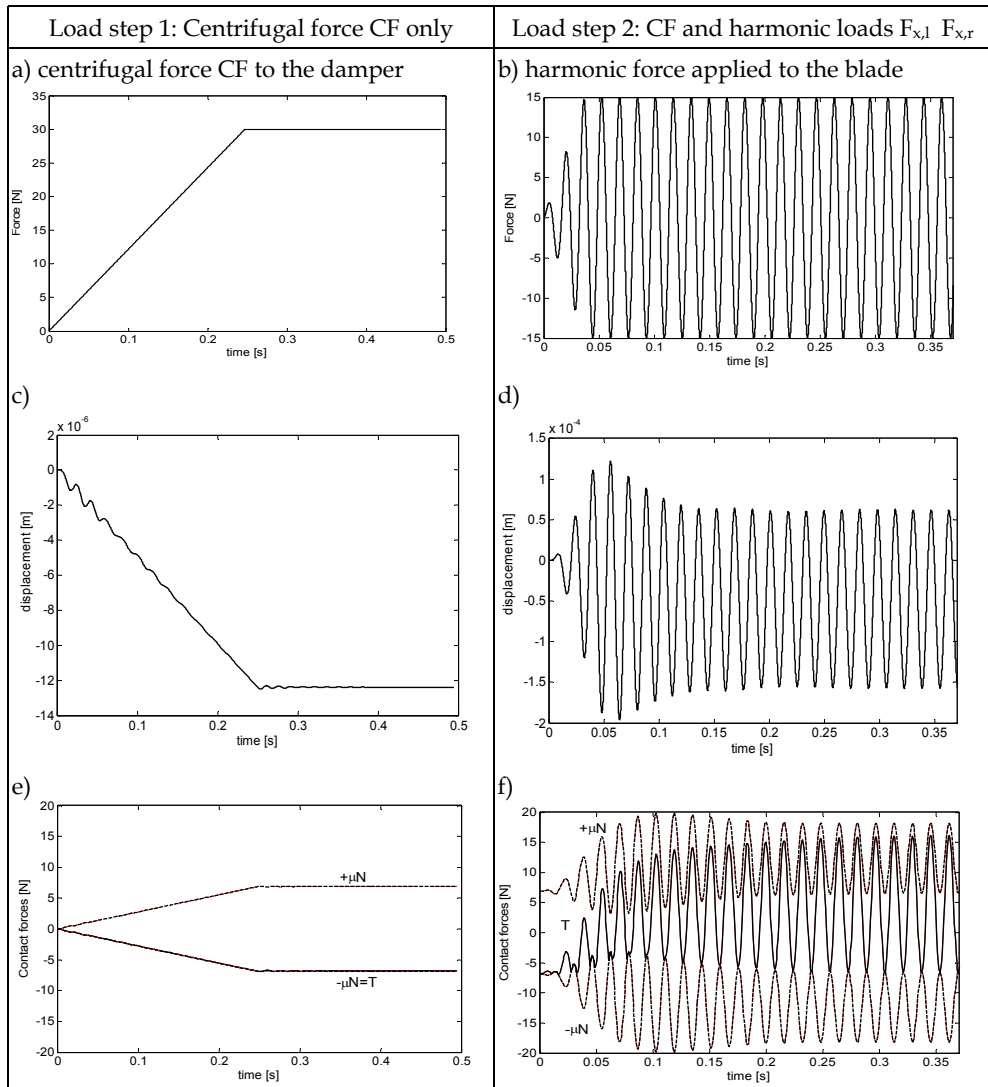| Load step 1: Centrifugal force CF only	Load step 2: CF and harmonic loads $F_{x,l}$ $F_{x,r}$
a) centrifugal force CF to the damper	b) harmonic force applied to the blade

Fig. 13. DTI of the blade-to-blade damper system: load step 1 (left) and load step 2 (right).

The quasi-static application of the centrifugal force in the first load step gives a value of the tangential contact force T equal to –μN at the end of the simulation. The force distribution corresponding to the static equilibrium at the end of the first load step is shown in Fig. 14. At the end of the second load step it is possible to see that the underplatform damper is fully stuck since the tangential relative motion at the contacts is not large enough to cause the slip of the surfaces. The stick state is visible in Fig. 13f since the tangential contact force T is not large enough to cross the boundary limit ±μN. In particular, T is tangent only to the lower boundary limit –μN. It must be finally highlighted that, when the steady-state response is reached at the end of the second load step, the static value of the normal and tangential forces changed with respect to the static values at the end of the first load step: the static normal load nearly doubled changing from 14N to 25N while the static tangential force increased from -7N to 4N.
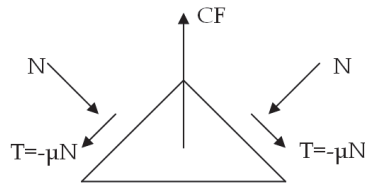

Fig. 14. Forces distribution on the damper after load step 1

This is a clear example of how the static contact forces over the contacts, both normal and tangential, are strongly influenced by the dynamics of the system and in general are not equal to the contact forces that can be carried out by the calculation of a static equilibrium of the structure.

4.2 Forced response in the frequency domain: the static/dynamic coupling of the balance equations and comparison with the uncoupled approach

The solution of the equilibrium equations using the direct time integration is usually a prohibitive approach for industry due to the large number of dofs used to model the complexity of a real component, in particular when the time is compared with the time-to-market constraints. For these reasons the HBM is a valuable tool based on the approximation of the time-depending quantities to their first harmonics according to the Fourier series approximation (see Section 2). The commonest approach that is found in literature and in the industry applications to solve iteratively the set of Equations (8) is based on the algorithm shown in Fig. 15a.

It is possible to see that the contact model employed within the algorithm needs a static normal load as an input parameter as already explained in Section 3. The relative motion between the mating surfaces is then processed within the contact model with the static normal load chosen a priori in order to calculate the contact forces.

Unfortunately, this approach may result not reliable if the choice of N_0 is based on a static equilibrium of the structure as proved in Section 4.1. Sometimes, as demonstrated in (Zucca et al., 2008), the range of possible solutions that can be obtained by assuming different conditions for the static equilibrium is so large that the simulation is not useful to assess the damping effectiveness. In order to avoid a preliminary static calculation of the contact forces, the authors presented a refined contact model (Firrone et al, 2011) which couples the static and dynamic equilibrium of the structure. The basic idea is to link the normal and

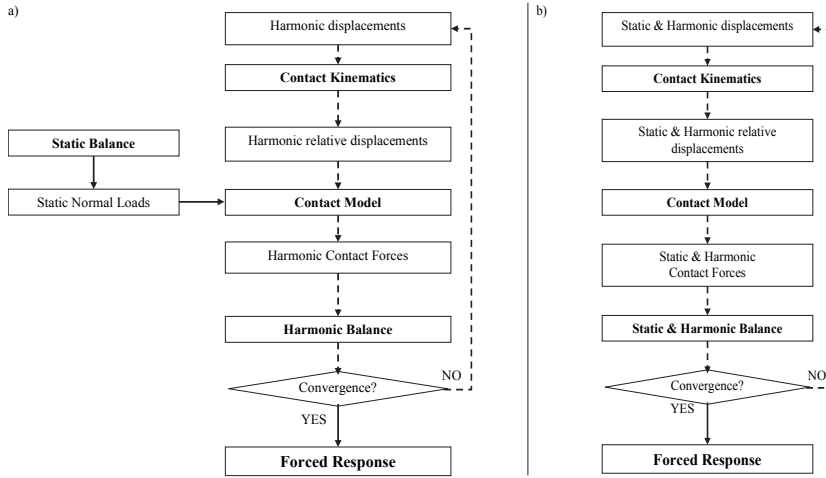a)   b)

Fig. 15. Uncoupled (a) and coupled (b) algorithms for the forced response calculation

tangential static contact forces directly to the normal and tangential static relative displacements $u^{(0)}$, $v^{(0)}$ at the contacts. In this case the quantities $u(t)$, $v(t)$, $u^{(0)}$, $v^{(0)}$ are the input data of the contact model instead of $u(t)$, $v(t)$ and N_0. In detail, instead of using Equation (13) based on a value of N_0 that is chosen a priori, $N(t)$ is defined as

$$N = \max \left[k_n \cdot v(t), \, 0 \right] = \max \left[k_n \cdot \Delta + k_n \cdot v^{(0)} + k_n \cdot \Re\left(v^{(n)} \cdot e^{i \cdot n \cdot \omega \cdot t} \right), \, 0 \right], \tag{24}$$

being Δ the design value of interference ($\Delta > 0$) or gap ($\Delta < 0$) existing between the contact points before the external forces act on the system.

The static component of the contact normal load $N^{(0)}$, necessary to compute the periodic tangential load $T(t)$, is directly linked to the static component of the normal relative displacement of the bodies in contact $v^{(0)}$ and to the interference (or gap) Δ. The influence of a static relative displacement $u^{(0)}$ over the contact plane on the determination of $T(t)$ is now discussed. If during one period of oscillation the contact enters the slip-state or the lift-off state, it can be demonstrated that the static value $T^{(0)}$ of the tangential contact force $T(t)$ is unique. This is also visible by looking at the hysteresis loop of Fig. 7 where, once the variable quantities $u(t)$ and $v(t)$ are determined as well as $N(t)$ according to Equation (24), also the static value $T^{(0)}$ is directly determined. On the contrary, if the contact is fully stick, more than one solution exists. A clear example is visible in Fig. 13 f where the tangential contact force $T(t)$ can vary being tangent either to μN or to $-\mu N$ according to the limits given by the Coulomb's law. All the other solutions, where $T(t)$ is in the middle of the two limits, are valid solutions as well. As a consequence, the static value $T^{(0)}$ is bounded within two values:

$$T_{\min}^{(0)} \leq T^{(0)} \leq T_{\max}^{(0)} \tag{25}$$

where $T^{(0)}_{\min}$ and $T^{(0)}_{\max}$ correspond to $T^{(0)}$ when $T(t)$ is tangent respectively to $-\mu N$ and μN (in the example of Fig. 13f it is $T^{(0)} = T^{(0)}_{\min} = 4N$).

In order to determine only one trend for $T(t)$ even in case of a fully stick contact, the following predictor/corrector procedure is used: first $T(t)$ is computed as

$$T = k_t \cdot u(t) = k_t \cdot u^{(0)} + k_t \cdot \Re\left(u^{(n)} \cdot e^{i \cdot n \cdot \omega \cdot t}\right), \qquad (26)$$

where $T^{(0)}$ is directly determined by the relative tangential displacement $u^{(0)}$. If T crosses the upper limit μN, then T is corrected as

$$T(t) = T_{max}^{(0)} + k_t \cdot \Re\left(u^{(n)} \cdot e^{i \cdot n \cdot \omega \cdot t}\right), \qquad (27)$$

while if T crosses the lower limit -μN, T is corrected as

$$T(t) = T_{min}^{(0)} + k_t \cdot \Re\left(u^{(n)} \cdot e^{i \cdot n \cdot \omega \cdot t}\right), \qquad (28)$$

otherwise T is not modified.

A consequence of the refined method is that the static displacements becomes part of the set of unknowns which must be calculated within the algorithm (Figure 15 b) and the static equilibrium using the 0-th term of the Fourier series of the displacements and contact forces must be considered as well as the other n harmonics.

The same dynamic problem of Fig. 12, solved in the former section by means of the DTI, is now solved in the frequency domain using the HBM (see Section 2) according to two strategies:

1.   Forced response calculation in the frequency domain (HBM), single harmonic (n=1), uncoupled approach (Algorithm of Fig. 15a).
2.   Forced response calculation in the frequency domain (HBM), single harmonic (n=1), static/dynamic coupling approach (Algorithm of Fig. 15b).

Equation (8) is solved iteratively with the Newton-Raphson non-linear solver. In this case the sub-set of non-linear degrees of freedom is:

$$Q_{NL}^{(n)} = \begin{bmatrix} q_{x1,l}^{(n)} & q_{y1,l}^{(n)} & q_{x1,r}^{(n)} & q_{y1,r}^{(n)} & q_{x,d}^{(n)} & q_{y,d}^{(n)} & \vartheta_d^{(n)} \end{bmatrix} \qquad (29)$$

Similarly to Equation (22) the harmonic relative displacements $u_L^{(n)}$, $u_R^{(n)}$, $v_R^{(n)}$ and $v_L^{(n)}$ at the contacts are computed by means of equation (22), where the time-dependent quantities are substituted by the n harmonics approximating the real motion. In this case only the first term of the Fourier series is considered. If the uncoupled approach is adopted different strategies can be used to choose the normal pre-load N_0. In (Petrov & Ewins, 2007), for instance, the static equilibrium of the damper is solved assuming the same force distribution shown in Figure 14, i.e., two contacts in slip state. In this case, in fact, the four unknown contact forces ($N_{0,l}$, $N_{0,r}$, $T_{0,l}$, $T_{0,r}$) are reduced to only two since the friction forces are equal to the Coulomb's lower limit. Two equilibrium equations along the horizontal and vertical translation are sufficient to calculate the static normal loads easily. Another hypothesis is assumed in (Panning et al., 2004) where the contact is assumed frictionless, i.e., $T_{0,l}=T_{0,r}=0$. In other cases a quasi-static analysis is performed within in-house software (Cigeroglu et al., 2009) in order to find the normal load distribution when the contacts are more than one per side. This approach is closer to the industrial practice of performing the same simulation with FE commercial software (Szwedowicz et al., 2008). In this case, the static normal loads are introduced by considering the force distribution of Figure 14 that is also the final result of the DTI at the end of the first load step (N_0=25N). The variable normal load N(t) is then written as in Equation (17) according to the uncoupled approach.

Unfortunately, different hypotheses about the normal pre-load lead to different amount of damping generated by the contacts and to different forced responses. To this end, the

static/dynamic coupling of the non-linear equilibrium equations is used in order to obtain unique solution in the frequency domain. The two calculations are repeated for a range of frequencies including the first natural frequency of the blades. Fig. 16a shows the forced response in terms of vibration amplitude of the tip of the left blade (mass m_2). The dashed line is the free response of the blade without the underplatform damper (linear calculation), square marks are the responses of the blade computed with the DTI for different excitation frequencies (non-linear calculation).
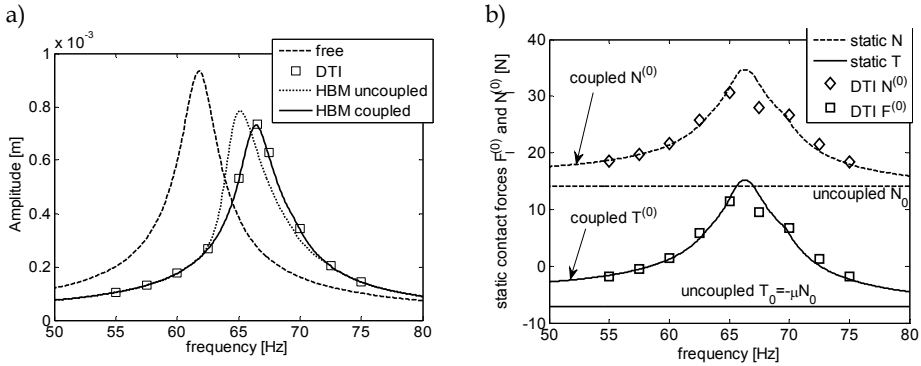

Fig. 16. (a) Comparison of the forced responses of the left blade calculated by means of different strategies (DTI vs. HBM) and (b) corresponding static contact forces on the damper

It is observed that the peak response shifts towards a higher frequency value since the contact with the damper is an additional constraint which stiffens the blade. At the same time, the peak amplitude decreases due to the damping introduced by friction. The dotted line is the non-linear response calculated by means of the uncoupled algorithm of Fig. 15a. Both the peak amplitude and the corresponding frequency are not correctly predicted. Finally, the solid line is the non-linear forced response of the left blade using the static/dynamic coupled approach (Figure 15 b). It is possible to see that the coupled solution perfectly matches the DTI of the equilibrium equations (20). The static normal loads of the left blade for the three different cases are reported in Fig. 16b. The markers are the static contact forces calculated by means of the DTI (diamond markers correspond to the static normal load while square markers are the static tangential force). The dashed and the solid lines refer respectively to the static normal and tangential loads when the HBM is used. The two horizontal trends are the static normal (N_0) and tangential (T_0) values that are chosen a priori within the uncoupled approach. Of course they are two constant values with respect to the excitation frequency since they are assumed regardless of the system dynamics. On the contrary, a good correspondence is found between the DTI method and the prediction of the static contact forces $N^{(0)}$ and $T^{(0)}$ when the static/dynamic coupled approach is used.

The linearization based on the first term of the Fourier series is not always sufficient to represent adequately the non-linear forced response of structures with friction damping. In particular, when the nonlinearities become larger and larger, more than one harmonic may be suitable to model the system dynamics. In the following example the stiffness k_x which links the mass m_1 to the mass m_2 is changed to 5.84e4 and the excitation forces on the blades have been increased to $F_{x,l}=F_{x,r}=30N$ in order to generate more slipping at the contacts. The forced response of the modified blades is then calculated by means of the DTI and the static/dynamic approach using one and three harmonics ($N_H=1, 3$).
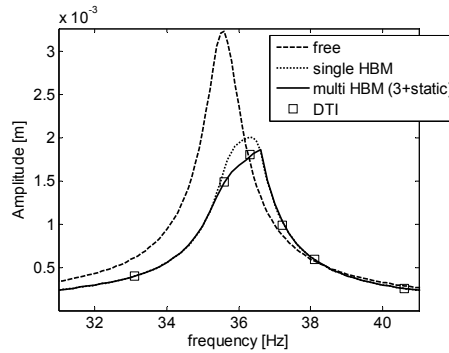
Fig. 17. Static/dynamic coupled approach, comparison of single and multi-HBM with DTI

The three results are shown in Fig. 17 for the sake of comparison, together with the free response of the blade. It is possible to see in this case that if only one harmonic of the Fourier series is retained the blade response is overestimated while three harmonics are sufficient to generate a more correct response.

Anyway, it was proved that in practical applications (Petrov & Ewins, 2005; Petrov, 2007) the additional contributions given by harmonics higher than the first one can be mostly neglected since their amplitude can be two or more orders of magnitudes below the amplitude of the fundamental harmonic. However, they may be important if the excitation is the sum of different loads vibrating at multiple values of frequencies.

5. Full scale applications

5.1 Reducing the size of the non-linear system

The solution of the balance equations (8) in the frequency domain can be a formidable task even with the newest computers in case of industrial applications, since the finite element models can be made of thousands, even millions of dofs. In order to reduce the long computation times, reduction techniques are applied to equations (8) and then the non-linear reduced model is solved with iterative methods, typical of non-linear algebraic equations. In the field of turbomachinery, in particular in the field of bladed disk dynamics, the first reduction technique consists in the application of the boundary conditions of cyclic symmetry (Petrov, 2004; Siewert et al., 2010).

5.1.1 Cyclic symmetry

When a rotating bladed disk is made of N_S identical sectors, it is not necessary to model the whole bladed disk to perform its dynamic analysis. It is possible to model only one of the sectors of the bladed disk, hence called fundamental sector, and then to apply the cyclic symmetry boundary conditions to the boundary nodes of the sector, where it would be connected with the adjacent sectors.

The dofs of the fundamental sectors can be divided into inner dofs Q_I, left dofs Q_L and right dofs Q_R. The first set includes all the dofs lying inside of the fundamental sector, while the second and the third includes dofs lying at the sector left and right boundary respectively, where the sector would be connected to adjacent sectors.

Then, since in cyclic symmetric structures under rotating excitation, like bladed disks, all the sectors vibrate with the same amplitude but with a phase delay depending on the angular speed of the rotor and on the harmonic order of the excitation forces, the following relationship holds for the arbitrary n^{th} harmonic component

$$Q_L^{(n)} = Q_R^{(n)} \cdot e^{in\phi} \tag{31}$$

where n is the generic harmonic index of the periodic rotating excitation and of the response and $\phi = 2\pi/N_S$ is the physical angle between two consecutive sectors of the bladed disk.

The use of the cyclic symmetry, when possible, reduces the size of the non-linear system of N_S times, with respect to the full system.

After the application of the cyclic symmetry, the balance equations of the fundamental sector are

$$D^{(n)} \cdot Q^{(n)} = F_E^{(n)} + F_{NL}^{(n)} \text{ with n = 0..N}_H \tag{32}$$

where $D^{(n)} = -(n\omega)^2 M^{(n)} + in\omega C^{(n)} + K^{(n)}$ is the n-th dynamic stiffness matrix of the system and $M^{(n)}$, $C^{(n)}$ and $K^{(n)}$ the mass, damping and stiffness matrices of the fundamental sector obtained applying the nth boundary conditions of equation (31).

5.1.2 Modal superposition

Even after the application of the cyclic symmetry boundary conditions of equation (31), the size of the nonlinear system can be too large for a solution in a reasonable amount of time.

One of the possible strategies to further reduce the number of the equations, is to write the balance equations (6) in modal coordinates (Panning et al. 2003; Cigeroglu et al., 2009). The first step is a modal analysis of the linear system without contact elements, to generate the eigenvalues and the eigenvectors of the system. It is a rather simple step which can be easily performed with any commercial finite element solver available.

As a result of this step, the harmonic components $Q^{(n)}$ of the physical displacements are defined as

$$Q^{(n)} = \Psi^{(n)} \cdot \eta^{(n)} \tag{33}$$

where $\eta^{(n)}$ are the modal amplitudes and $\Psi^{(n)}$ are the mass-normalized mode shapes obtained solving the following eigen-problem

$$\det(K^{(n)} - \lambda M^{(n)}) = 0 \tag{34}$$

Being $K^{(n)}$ and $M^{(n)}$ the stiffness and the mass matrices of the fundamental sector with the cyclic symmetry boundary conditions of equation (31).

The physical balance equations (6) are then replaced by the modal balance equations

$$\eta^{(n)} = \eta_E^{(n)} + \alpha^{(n)} \cdot \varphi_{NL}^{(n)} \tag{35}$$

where $\eta_E^{(n)}$ is the linear response due to the external forces, $\alpha^{(n)}$ the modal receptance matrix and $\varphi_{NL}^{(n)}$ the modal non-linear forces due to friction contacts.

In order to include in the solution process the contact models described in Section 3, based on the procedure depicted in Fig. 2, transitions from the modal to the physical domain and

vice versa are necessary. Physical displacements of contact nodes $Q_{NL}^{(n)}$ are computed by equation (33), while physical contact forces $F_{NL}^{(n)}$ generated at the contact nodes are transformed in the modal forces $\varphi_{NL}^{(n)}$ of equation (35) by

$$\varphi_{NL}^{(n)} = \Psi^{(n)H} \cdot F_{NL}^{(n)} \tag{36}$$

where the superscript H denotes the Hermitian, or complex conjugate, operator.

The main advantage of modal superposition is that the size of the reduced model of equation (35) does not depend on the number of contact points but on the number of mode shapes retained to describe the dynamics of the system. On the other hand, if friction contacts modify strongly the dynamics of the bladed disk, the number of mode shapes necessary to represent accurately its dynamics could be relatively large. It is the case, for instance, of shrouded blades, where the friction contacts are located at the blade tip. In this case, the dynamics of the shrouded blade is completely different from the dynamics of the cantilevered free blade, used to extract the modal parameters in equation (34).

5.1.3 Component mode synthesis

When modal superposition is an unfeasible approach due to the large number of mode shapes necessary to represent accurately the dynamics of the system, a model reduction based on component mode synthesis (CMS) (Craig & Bampton, 1968) is possible.

The dofs $Q^{(n)}$ of the system can be partitioned into master dofs $Q_M^{(n)}$, and slave dofs $Q_S^{(n)}$. As a result, the homogeneous undamped linear system associated to the n-th harmonic order becomes

$$\left(\begin{bmatrix} K_{MM}^{(n)} & K_{MS}^{(n)} \\ K_{SM}^{(n)} & K_{SS}^{(n)} \end{bmatrix} - \omega^2 \begin{bmatrix} M_{MM}^{(n)} & M_{MS}^{(n)} \\ M_{SM}^{(n)} & M_{SS}^{(n)} \end{bmatrix} \right) \cdot \begin{Bmatrix} Q_M^{(n)} \\ Q_S^{(n)} \end{Bmatrix} = \begin{Bmatrix} 0 \\ 0 \end{Bmatrix} \tag{37}$$

The physical vector of dofs $Q^{(n)}$ is then approximated by a linear superposition of static modes and of slave mass-normalized mode shapes.

The first step of the procedure is based on the static reduction of the homogenous system

$$\begin{bmatrix} K_{MM}^{(n)} & K_{MS}^{(n)} \\ K_{SM}^{(n)} & K_{SS}^{(n)} \end{bmatrix} \begin{Bmatrix} Q_M^{(n)} \\ Q_S^{(n)} \end{Bmatrix} = \begin{Bmatrix} 0 \\ 0 \end{Bmatrix} \tag{38}$$

which leads to the following expression

$$\begin{Bmatrix} Q_M^{(n)} \\ Q_S^{(n)} \end{Bmatrix} = \begin{Bmatrix} I \\ K_{MM}^{(n)} - K_{MS}^{(n)} \cdot K_{SS}^{(n)-1} \cdot K_{SM}^{(n)} \end{Bmatrix} Q_M^{(n)} \tag{39}$$

where I is the identity matrix.

The second step consists in the calculation of the slave eigenvectors $\Psi_S^{(n)}$ computed solving the eigenproblem

$$\det(K_{SS}^{(n)} - \lambda M_{SS}^{(n)}) = 0 \tag{40}$$

and giving the relationship

$$Q_S^{(n)} = \Psi_S^{(n)} \cdot \eta_S^{(n)} \,. \tag{41}$$

By linear combination of equations (39) and (41), the physical dofs are expressed as

$$Q^{(n)} = \begin{Bmatrix} Q_M^{(n)} \\ Q_S^{(n)} \end{Bmatrix} = \begin{bmatrix} I & 0 \\ K_{MM}^{(n)} - K_{MS}^{(n)} \cdot K_{SS}^{(n)-1} \cdot K_{SM}^{(n)} & \Psi_S^{(n)} \end{bmatrix} \cdot \begin{Bmatrix} Q_M^{(n)} \\ \eta_S^{(n)} \end{Bmatrix} = \Phi_{CMS}^{(n)} \cdot \begin{Bmatrix} Q_M^{(n)} \\ \eta_S^{(n)} \end{Bmatrix} = \Phi_{CMS}^{(n)} \cdot q^{(n)} \tag{42}$$

The resulting reduced model has the following balance equations

$$d^{(n)} \cdot q^{(n)} = f_E^{(n)} + f_{NL}^{(n)} \quad \text{with n = 0..N}_H \tag{43}$$

where $d^{(n)} = -(n\omega)^2 m^{(n)} + in\omega c^{(n)} + k^{(n)}$ is the n-th dynamic stiffness matrix of the system and $m^{(n)}$, $c^{(n)}$ and $k^{(n)}$ are the reduced mass, damping and stiffness matrices defined as

$$k^{(n)} = \Phi_{CMS}^{(n)}{}^H \cdot K^{(n)} \cdot \Phi_{CMS}^{(n)}; \quad c^{(n)} = \Phi_{CMS}^{(n)}{}^H \cdot C^{(n)} \cdot \Phi_{CMS}^{(n)}; \quad m^{(n)} = \Phi_{CMS}^{(n)}{}^H \cdot M^{(n)} \cdot \Phi_{CMS}^{(n)}; \tag{44}$$

while the reduced forces are defined as $f_E^{(n)} = \Phi_{CMS}^{(n)}{}^H \cdot F_E^{(n)}; \quad f_{NL}^{(n)} = \Phi_{CMS}^{(n)}{}^H \cdot F_{NL}^{(n)}$

The correct strategy to implement the CMS technique to non-linear systems with friction contacts is to include the non-linear contact dofs $Q_{NL}^{(n)}$ in the set of master nodes. In this way, the physical displacements necessary to compute the contact forces $F_{NL}^{(n)}$ are explicitly included in the set of the unknowns of the reduced model and transition from the generalized to the physical coordinates and vice versa is not necessary during the calculation. Furthermore, as for the case of modal superposition, the CMS is a rather simple step which can be easily performed with any commercial finite element solver.

5.2 Modeling microslip

Contact elements described in Section 3 and used to model periodical contact forces at friction contacts assume an ideal gross-slip behavior of the contact. Once the modulus of tangential force T equals the Coulomb limit value µN, the contact enters the slip state.

Real contacts in industrial application are mostly conforming contact and the contact extends on a finite contact area larger than a single point. In these conditions, the transition between full sticking and slipping conditions is not so abrupt as modeled in Section 3. First of all, the outer parts of the contact surfaces enter the slipping conditions while the inner parts are still sticking. Then as the tangential contact load grows larger, the slipping area extends progressively to the whole contact area and gross slip occurs. The transition state between the sticking and the gross slipping conditions is called microslip (Filippi et al., 2004; Cigeroglu et al., 2007; Allara, 2009). It is an important contact state, since most of the friction contacts in industrial application works in microslip conditions.
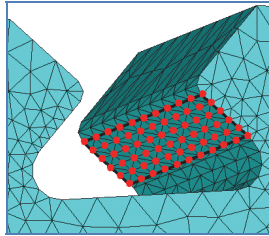

Fig. 18. Contact points of a blade root joint on a bladed disk

In order to model the microslip behavior of friction contacts in numerical simulations of frictionally damped structures, the contact area is divided into a grid made of several contact points, as shown in Fig. 18, where red points are used to identify the contact points on a bladed disk at the blade root joint.

Then the contact parameters (tangential and normal contact stiffness) are evaluated for the whole contact (Allara, 2009) and their value is evenly distributed among the contact nodes.

5.3 Case studies

The static/dynamic coupled approach described in Section 4.2, is now applied to two case studies, representing two of the most typical configurations of friction contacts in bladed disks: blade root joints and underplatform dampers.

5.3.1 Blade root joint

This application is very common in turbine bladed disks because the blades are connected to the disk rim by means of firtree or dovetail roots, inserted in the corresponding disk slots. In this case, the friction damping is generated at the contact between the blade root and the disk slot during the vibration of the assembly. The material of the mock bladed disk (Fig. 19) used for the analysis is steel and the number of blades is 12. The disk and the blades are modeled with the finite element method. Cyclic symmetry boundary conditions are applied to the disk, in order to model only its fundamental sector, while the blade is modeled with free-free boundary conditions.

Both the blade and the disk sector models are then reduced by means of the modal superposition principle. Each pair of contact nodes lying on the blade/disk interface are connected by means of two orthogonal 1D contact elements, taking into account variable normal load (See section 4.2).
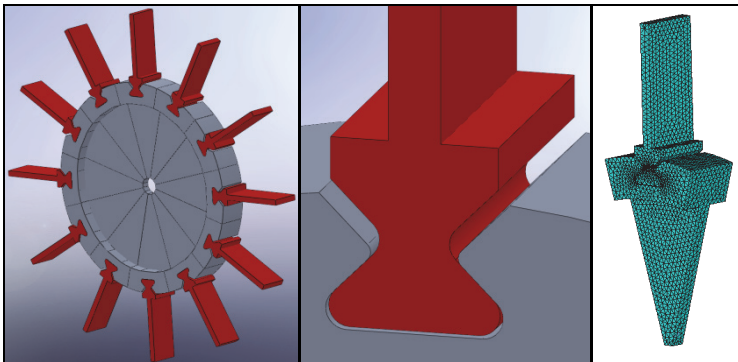

Fig. 19. Mock bladed disk: full view, detail of the root joint, finite element model.

The forced response of the system around the 1st bending mode of the blades with 6 nodal diameters is studied, corresponding to the out-of-phase vibration of two consecutive blades, using the 0th and the fundamental order of the Fourier terms.

The contact between the blade and the disk rim occurs when the bladed disks rotates and the centrifugal force presses the blade root onto the disk slots, the value of the design interference Δ is set equal to zero. The friction coefficient μ is set equal to 0.5 and the values

of normal and tangential contact stiffness are computed assuming a flat punch contact (Allara, 2009) and are evenly distributed among the contact nodes.
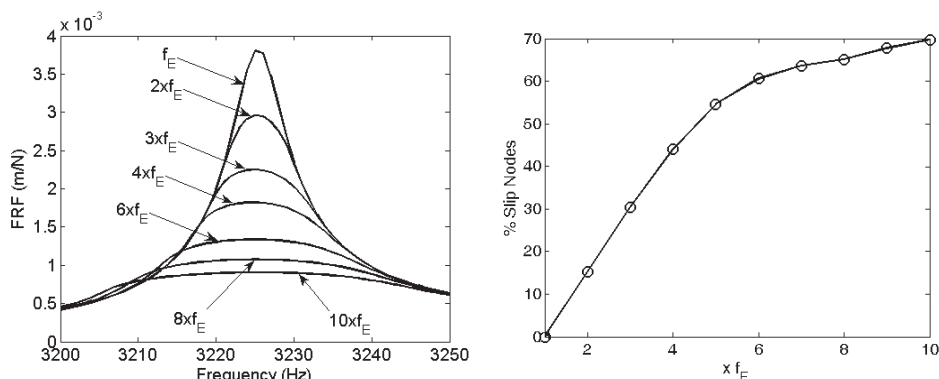

Fig. 20. Blade root joint: Forced response of the blade and slip growth.

The frequency response function (FRF) of the system, computed for different amplitudes of the engine order excitation, is shown in Fig. 20. The non-linear behavior of the blade root joint is evident, as the FRF of the system decreases as the amplitude of the excitation grows larger. At the lowest amplitude, the contact surfaces are fully stuck, while as the excitation force increases, slip begins at the boundary of the contact area and extends inward, as shown in Fig. 20, where the growth of the slipping area in percentage with respect to the total contact area is plotted.

5.3.2 Underplatform damper

The second application is an integral bladed disk (a.k.a. blisk) with underplatform dampers (Fig. 21). The dampers are wedge shaped devices located under the blade platforms and held in contact with them by the centrifugal force acting on the dampers themselves during rotation. Friction damping is generated at the contact surface between the left (L) and the right (R) damper surfaces and the walls of the blade cavities. Also in this case, the value of the design interference Δ is set equal to zero, since contact occurs only when the centrifugal force acts on the damper.
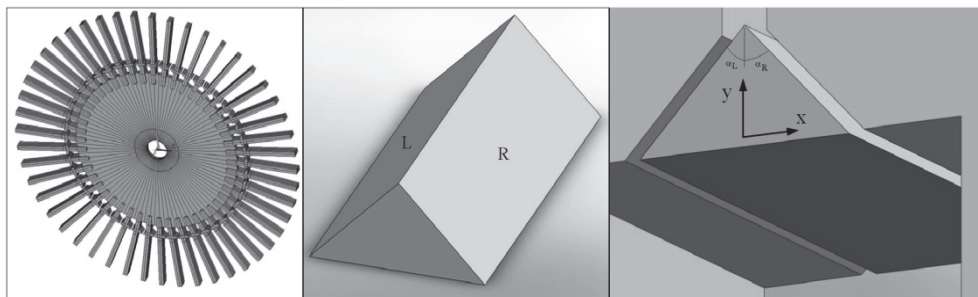

Fig. 21. Blisk geometry, damper geometry and damper location under the blade platforms.

Underplatform dampers are included in the design of turbine bladed disks as a system of passive control of vibration, when the detuning of the system is not possible, due to the high modal density of the bladed disk and/or to the wide spectrum of the excitation forces.

The material of the blisk and of the dampers is steel, the number of blades is 48, the damper is symmetrical with $\alpha_L = \alpha_R = 45°$, the friction coefficient is set to $\mu = 0.5$; the contact parameters k_t and k_n are computed assuming a flat punch contact (Allara, 2009) and then uniformly distributed over the contact nodes.

The blisk and the dampers are modeled with the finite element method. Cyclic symmetry boundary conditions are applied to the blisk, in order to model only one fundamental sector, while the damper is modeled with free-free boundary conditions. The modal superposition principle is used to reduce the size of the models and the 0th and 1st order harmonics are used in the analysis.

The effect of the main damper design parameter, the damper mass, on the dynamics of the assembly is investigated around the 1st bending mode shape of the blades, in case of 12th engine order excitation.

The FRF curves of the system are plotted in Fig. 22, where the effect of the damper mass on the system dynamics, both in terms of vibration amplitude and resonance frequency can be observed. An optimum damper mass exists and corresponds to the minimum vibration amplitude, while as the damper mass grows larger than the optimum value, the system response increases again and stabilizes when full sticking conditions are established. A full resume of the effect of the damper mass on the system response is shown in terms of the damper optimization curve, in Fig. 22.

As described in Section 5.2, in order to model microslip, the contact area is meshed with a regular grid of contact nodes. In Fig. 23, the evolution of the contact status versus the value of the damper mass is shown.
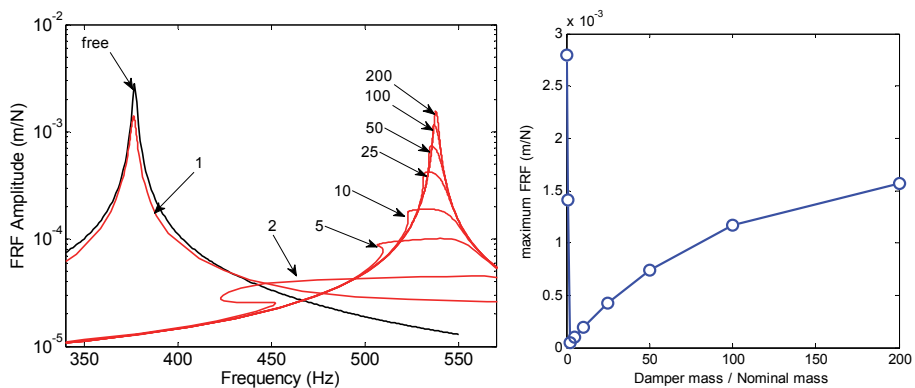

Fig. 22. Effect of the damper mass ($m_d = n \times m_{nom}$ with n = [1:200].): FRF curves (left) and optimization plot (right).

The FRF curves refer to a damper mass 25, 50, 100 and 200 times the nominal mass (m_{nom}). The status of the contact area is shown by means of the following colors (white: sticking; grey: alternate stick-slip; black: partial lift-off). The plots show that at 200x the contact is almost fully stuck, while the microslip increases as the damper mass becomes lower. At 25x no sticking areas are found and only alternating stick-slip and partial lift-off occur. The plots

also show that the upper part of the contact is subjected to partial lift-off in the whole range of explored damper masses, due to the blade platform kinematics, characterized by larger displacements at the higher radius.
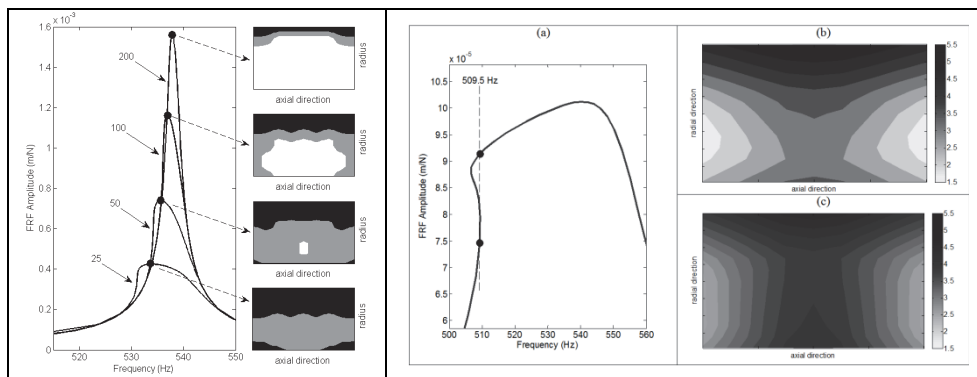

Fig. 23. Effect of the damper mass on the contact status (left). Different distributions of static normal load in case of coupled static/dynamic calculation (right).

On the right-hand side of Fig. 23, the FRF curve corresponding to 5x damper mass is shown. At 509.5 Hz multiple solution exist due to the softening effect produced by the partial lift-off of the contact surfaces. Two solutions are highlighted by the black points over the FRF curve. The distributions of static normal loads predicted at the upper point (b) and at the lower point (c) are also plotted. They differ to each other, despite being computed at the same frequency, i.e. at the same rotational speed and at the same centrifugal force. This result is possible only if the static and the dynamic contact forces acting on the damper are computed simultaneously as proposed with the coupled approach described in Section 4.2. In case of preliminary static analysis, the same distributions of static normal loads would be predicted.

6. Conclusions

One of the emerging directions in the design of complex structures is the modeling of joints. Today, friction contacts are one of the key phenomena to understand in order to predict correctly the dynamics of assemblies and the corresponding stress distribution. In the last two decades companies were more and more interested in including the nonlinear action of sliding surfaces within the design procedure by means of time efficient numerical tools.

In this paper the consolidated procedure of solving the nonlinear equilibrium equations of the system by means of the Harmonic Balance Method (HBM) is therefore described. HBM has the advantage of reducing the calculation time in spite of an acceptable approximation of the forced response with respect to the integration of the differential equations in the time domain (DTI).

A review of the classical modeling of friction contacts is presented and the main parameters which i) correctly describe the slip/stick/separation phenomenon and ii) mainly affect the response of the bodies in contact are defined and commented. Particular attention is paid to show why one contact model shall be preferred in spite of others in practical applications where the fast computation of the forced response is an asset.

The strong influence of the dynamic response of the structure on the determination of the static loads acting at the contact (and vice versa) is proved through a simple lumped parameter model whose equilibrium is solved by DTI. The classical contact models are not sufficient to simulate this dependence since the normal load is a parameter chosen a priori which does not depend on the dynamics of the structure.

In order to take into account the mutual influence, the authors proposed an improved contact model which couples the static and the dynamic equilibrium equations of the system.

Simulations obtained with the classical and refined contact models both implemented in a HBM algorithm are compared to the DTI response and it is demonstrated that the coupling of the static and dynamic equilibrium equations of the structure is of primary importance to predict the maximum oscillation amplitude of the system (therefore the maximum stress concentration) and the stiffening of the structure due to the contacts.

Finally, two practical examples of the application of the refined contact model to turbomachinery components are presented where friction dampers are optimized for two bladed disks in order to reduce the blade vibrations.

7. Appendix - numerical methods and solver optimization

In order to solve the non-linear balance equations of vibrating structures with friction contact, iterative numerical method are necessary. In the technical literature, the most exploited method is the continuation method in two of its possible versions: natural continuation and arc-length continuation.

In this appendix, we consider the non-linear balance equations of the structure

$$Q_{NL}^{(n)} = Q_{E,NL}^{(n)} + R_{NL,NL}^{(n)} \cdot F_{NL}^{(n)} \tag{45}$$

as described in Section 2 of this chapter, but the contents of this appendix are still valid also in case of reduced order models. In order to solve the algebraic system (45), the complex equations are first of all turned into a set of real equations with real unknowns. So the following real quantities are defined

$$X = \left\{ Q_{NL}^{(0)}; \quad \Re\left(Q_{NL}^{(1)}\right); \quad \Im\left(Q_{NL}^{(1)}\right); \quad \cdots \quad \Re\left(Q_{NL}^{(N_H)}\right); \quad \Im\left(Q_{NL}^{(N_H)}\right) \right\} \tag{46}$$

$$X_E = \left\{ Q_{E,NL}^{(0)}; \quad \Re\left(Q_{E,NL}^{(1)}\right); \quad \Im\left(Q_{E,NL}^{(1)}\right); \quad \cdots \quad \Re\left(Q_{E,NL}^{(N_H)}\right); \quad \Im\left(Q_{E,NL}^{(N_H)}\right) \right\} \tag{47}$$

$$F_X = \left\{ F_{NL}^{(0)}; \quad \Re\left(F_{NL}^{(1)}\right); \quad \Im\left(F_{NL}^{(1)}\right); \quad \cdots \quad \Re\left(F_{NL}^{(N_H)}\right); \quad \Im\left(F_{NL}^{(N_H)}\right) \right\} \tag{48}$$

$$R_X = \begin{bmatrix} R_{NL,NL}^{(0)} & 0 & 0 & \cdots & 0 & 0 \\ 0 & \Re\left(R_{NL,NL}^{(1)}\right) & -\Im\left(R_{NL,NL}^{(1)}\right) & \cdots & 0 & 0 \\ 0 & \Im\left(R_{NL,NL}^{(1)}\right) & \Re\left(R_{NL,NL}^{(1)}\right) & \cdots & 0 & 0 \\ \vdots & \vdots & \vdots & \ddots & \vdots & \vdots \\ 0 & 0 & 0 & \cdots & \Re\left(R_{NL,NL}^{(N_H)}\right) & -\Im\left(R_{NL,NL}^{(N_H)}\right) \\ 0 & 0 & 0 & \cdots & \Im\left(R_{NL,NL}^{(N_H)}\right) & \Re\left(R_{NL,NL}^{(N_H)}\right) \end{bmatrix} \tag{49}$$

and the balance equations to solve become

$$X = X_E + R_X \cdot F_X(X) \tag{50}$$

7.1 Natural continuation

In this case, we want to compute the response of the system in a given range of frequencies $[\omega_i, \omega_f]$ of the fundamental harmonics of the external excitation with a frequency resolution $\Delta\omega$.
The balance equation is written in the form f(X)=0 as

$$f(X) = X - X_E - R_X \cdot F_X(X) = 0 \tag{51}$$

The analysis starts at $\omega = \omega_i$ with a guess value X_0, for instance the value of the response of the linear system without fiction contacts, and a Newton-Raphson procedure is then initialized. At the generic step, the (k+1)[th] value is computed as

$$X_{k+1} = X_k - J(X_k)^{-1} \cdot f(X_k) \tag{52}$$

with the value of the functions f(X_k) defined as

$$f(X_k) = X_k - X_E - R_X \cdot F_X(X_k) = 0 \tag{53}$$

and the jacobian matrix J of the system defined as

$$J(X_k) = df(X)/dX\big|_{X=X_K} = I - R_X \cdot dF_X(X)/dX\big|_{X=X_K}. \tag{54}$$

When the norm of the residuals of f(X) is lower than a prescribed tolerance, the algorithm stops, the solution is saved and the frequency is increased to $\omega = \omega_i + \Delta\omega$. According to natural continuation, the guessed value at the generic frequency ω is the solution computed at $\omega - \Delta\omega$. In this way, the range of frequencies of interest is spanned with an ascending (or descending) order.
In order to improve the convergence of the algorithm and to shorten the calculation time, a feasible and effective option (Petrov & Ewins, 2003; Borrajo et al., 2006; Siewert et al, 2010) is the analytical calculation of the jacobian matrix J defined in equation (54). The key point is the analytical calculation of the derivatives of the Fourier coefficients of the non-linear contact forces dF_X/dX.

7.2 Arc-length continuation

When natural continuation is implemented, the range of frequencies of interest is spanned either with an ascending or with a descending order. In case of partial lift off of the contact points, the response curve may exhibit the so-called jump phenomenon, shown in Fig. 24. For a given frequency multiple solutions exist and turning points appear on the FRF curve where the resonance peaks shows either a hardening or a softening behavior. In these cases, the natural continuation approach is not able to follow the FRF curve and to compute the whole curve. A strategy based on two calculations, one with an ascending frequency order and the other with a descending frequency order, may partly help and compute both the lower and the upper branch of the solution but not the intermediate branch, shown in Fig. 24.
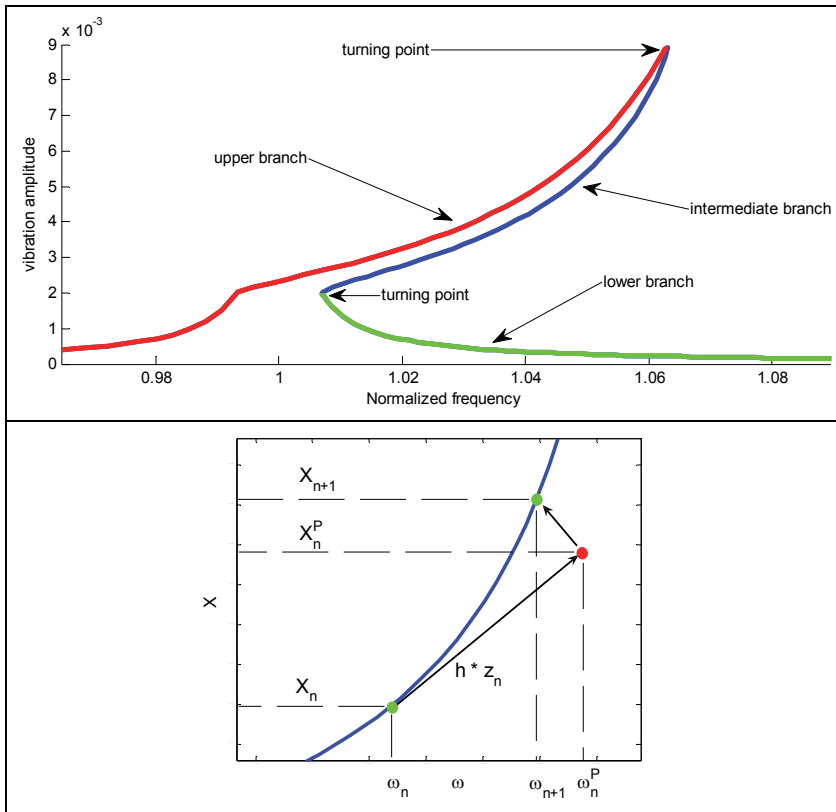
Fig. 24. Forced response curve with multiple solutions (top) and example of arc-length continuation (bottom).

In order to overcome this limitation of the natural continuation approach, an arc-length continuation method can be used (Chan & Keller, 1982), based on a predictor-corrector strategy. The first calculation at $\omega=\omega_i$ is performed with the classical Newton-Raphson method described in equation (52). Then (Fig. 24), the following arc-length continuation strategy can be used:

1. For a given n^{th} solution X_n at frequency ω_n, a predictor step is performed as

$$Y_n^P = \begin{Bmatrix} X_n^P \\ \omega_n^P \end{Bmatrix} = \begin{Bmatrix} X_n \\ \omega_n \end{Bmatrix} + h \cdot Z_n = Y_n + h \cdot Z_n \tag{55}$$

where Z_n is the unit vector tangent to the solution curve at the nth solution and h a scalar controlling the length of the predictor step.

2. A corrector step is implemented searching for the solution in a direction orthogonal to the predictor step. The augmented system of equations solved in the corrector step consists of the following equations

$$\begin{cases} X - X_E - R_X \cdot F_X(X) = 0 \\ Z_n^{\ T} \cdot \left(Y_n^P - Y \right) = 0 \end{cases} \tag{56}$$

including the balance equations (51) and the equation used to define the corrector step direction. As a consequence, also the vectors of the unknowns is augmented including also the excitation frequency ω. Equation (56) is solved with the Newton-Raphson method, starting with a guessed value equal to Y_n^P .

8. References

Allara M. (2009). A model for the characterization of friction contacts in turbine blades, *Journal of Sound & Vibration*, Vol.320, No.3, (February 2009), pp. 527-544, ISSN 0022-460X

Allara, M; Zucca, S.; Gola, M.M (2007). Effect of crowning of dovetail joints on turbine blade root damping, *Key Engineering Materials*, Vol. 347, (September 2007), pp. 317-322.

Awrejcewicz J.; Supeł B.; Lamarque C.-H.; Kudra G.; Wasilewski G. & Olejnik P. (2008). Numerical and experimental study of regular and chaotic motion of triple physical pendulum, *International Journal of Bifurcation and Chaos*, Vol.18, No.10, (October 2008), pp.2883-2915, ISSN 0218-1274

Awrejcewicz J.; Grzelczyk D. & Pyryev Yu. (2008b). A novel dry friction modeling and its impact on differential equation and Lyapunov exponents estimation, *Journal of Vibroengineering*, Vol.10, No.4, (December 2008), pp. 475-482, ISSN 1392-8716

Awrejcewicz J. & Pyryev Yu. (2009). *Nonsmooth Dynamics of Contacting Thermoelastic Bodies*, Springer-Verlag, ISBN 978-0-387-09652-0, New York

Borrajo J.M.; Zucca S. & Gola M.M. (2006). Analytical Formulation of the Jacobian Matrix for Non-linear Calculation of the Forced Response of Turbine Blade Assemblies with Wedge Friction Dampers, *International Journal of Non-linear Mechanics*, Vol.41, No.10, (December 2006), pp. 1118-1127, ISSN 0020-7462

Cardona, A.; Lerusse, A. & Geradin, M. (1998). Fast Fourier Nonlinear Vibration Analysis, *Computational Mechanics*, Vol.22, No.2, (August 1998), pp. 128-142, ISSN 0178-7675

Chan, T.F.C.; Kelle,r H.B. (1982). Arc-Length Continuation and Multi-Grid Techniques for Nonlinear Elliptic Eigenvalue Problems, *SIAM Journal of Scientific and Statistical Computing*, Vol.3, No.2, pp. 173-194, ISSN 0196-5204

Charleux, D.; Gibert, C.; Thouverez, F.; Dupeux, J. (2006). Numerical and experimental study of friction damping blade attachments of rotating bladed disks, *International Journal of Rotating Machinery*, vol. 2006, Article ID 71302.

Cigeroglu, E.; An, N. & Menq, C. H. (2007). A Microslip Friction Model with Normal Load Variation induced by Normal Motion, *Nonlinear Dynamics*, Vol.50, No.3, (November 2007), pp. 609-626, ISSN 0924-090X

Cigeroglu E.; An N. & Menq C.H. (2009). Forced Response Prediction of Constrained and Unconstrained Structures Coupled Through Frictional Contacts, *Journal of*

Engineering for Gas Turbines and Power, Vol.131, No.2, (March 2009), ISSN 0742-4795

Craig R.R. & Bampton M.C.C. (1968). Coupling of Substructures for Dynamic Analyses, *AIAA Journal*, Vol.6, No.7, pp.1313-1319, ISSN 0001-1452

Csaba, G. (1998). Forced Response Analysis in Time and Frequency Domains of a Tuned Bladed Disk with Friction Dampers, *Journal of Sound and Vibration*, Vol.214, No.3, (July 1998), pp. 395-412, ISSN 0022-460X.

Filippi S.; Akay A. & Gola M.M. (2004). Measurement of tangential contact hysteresis during microslip, *ASME Journal of Tribology*, Vol.126, No.3, (July 2004), pp.482–489, ISSN 0742-4787

Firrone C.M.; Botto D. & Gola M.M. (2006) Modelling A Friction Damper: Analysis Of The Experimental Data And Comparison With Numerical Results, (ESDA2006-95605), *Proceedings of ESDA 2006*, ISBN 0-7918-4250-9, Torino, Italy, July, 2006

Firrone C.M.; Zucca S. & Gola M.M. (2011). The effect of underplatform dampers on the forced response of bladed disks by a coupled static/dynamic harmonic balance method, *International Journal of Non-Linear Mechanics*, Vol.46, No.2, (March 2011), pp.363-375, ISSN 0020-7462

Griffin J.H. (1980). Friction damping of resonant stresses in gas turbine engine airfoils, *Journal of Engineering for Power*, Vol.102, No.2, pp.329-333, ISSN 0022-0825

Griffin J.H. & Menq C.H. (1991). Friction Damping of Circular Motion and Its Implications to Vibration Control, *Journal of Vibration and Acoustics*, Vol.113, No.2, (April 1991), pp.225-229, ISSN 1048-9002

Menq C.H. & Yang B.D. (1998). Non-Linear Spring Resistance and Friction Damping of Frictional Constraint having Two-Dimensional Motion, *Journal of Sound and Vibration*, Vol. 217, No.1, (October 1998), pp.127-143, ISSN 0022-460X

Panning L.; Sextro W & Popp K. (2003). Spatial Dynamics of Tuned and Mistuned Bladed Disks with Cylindrical and Wedge-Shaped Friction Dampers, *International Journal of Rotating Machinery*, Vol.9, No.3, (July 2002), pp.219-228, ISSN (printed): 1023-621X. ISSN (electronic): 1542-3034.

Panning L.; Popp K.; Sextro W.; Goetting F.; Kayser A. & Wolter I. (2004). Asymmetrical underplatform dampers in gas turbine bladings: theory and application, (GT2004-53316), *Proceedings of ASME Turbo Expo*, ISBN 0-7918-4171-5, Vienna, Austria, June, 2004

Petrov E.P. & Ewins D.J. (2003). Analytical formulation of friction interface elements for analysis of nonlinear multiharmonic vibrations of bladed discs, *Transactions of ASME Journal of Turbomachinery*, Vol.125, No.2, (April 2003), pp.364-371, ISSN 0889-504X

Petrov E.P. (2004). A method for use of cyclic symmetry properties in analysis of nonlinear multiharmonic vibrations of bladed disks, *Journal of Turbomachinery*, Vol.126, No.1, (January 2004), pp.175-183, ISSN 0889-504X

Petrov E.P. & Ewins D.J. (2006). Effects of damping and varying contact area at blade-disc joints in forced response analysis of bladed disk assemblies, *Journal of Turbomachinery*, Vol.128, No.2, (April 2006), pp. 403-410, ISSN 0889-504X

Petrov E.P. & Ewins D.J. (2007). Advanced Modeling of Underplatform Friction Dampers for Analysis of Bladed Disk Vibration, *Journal of Turbomachinery*, Vol.129, No.1, (January 2007), pp.143-150, ISSN 0889-504X

Petrov E.P. (2007). Explicit Finite Element Models of Friction Dampers in Forced Response Analysis of Bladed Discs, (GT2007-27980), *Proceedings of ASME Turbo Expo 2007*, ISBN 0-7918-4794-2, Montreal, Canada, May, 2007.

Sanliturk K.Y. & Ewins D.J. (1996). Modelling Two-Dimensional Friction Contact and its Application using Harmonic Balance Method, *Journal of Sound and Vibration*, Vol.193, No.2, (June 1996), pp.511-523, ISSN 0022-460X

Sanliturk K.Y.; Ewins D.J. & Stanbridge A.B. (2001). Underplatform Dampers for Turbine Blades: Theoretical Modelling, Analysis and Comparison with Experimental Data, *Journal of Engineering for Gas Turbines and Power*, Vol.123, No.4, (October 2001), pp.919-929, ISSN 0742-4795

Siewert C.; Panning L.; Wallaschek J. & Richter C. (2010). MultiHarmonic Forced Response Analysis of a Turbine Blading Coupled by NonLinear Contact Forces, *Journal of Engineering for Gas Turbines and Power*, Vol.132, No.8, (August 2010), ISSN 0742-4795

Srinivasan A.V., (1997). Flutter and Resonant Vibration Characteristics of Engine Blades, *Journal of Engineering for Gas Turbines and Power*, Vol. 119, No.4 (October 1997), pp. 742-775.

Szwedowicz J. (2008). Bladed disks: non linear dynamics, *Structural design of aircraft engines: key objectives and techniques*, E. Seinturier & G. Paniagua, ISBN 978-2-930389-8-2-6, Belgium

Szwedowicz J.; Gibert C.; Sommer T.P. & Kellerer R. (2008). Numerical and Experimental Damping Assessment of a Thin-Walled Friction Damper in the Rotating Setup with High Pressure Turbine Blades, *Journal of Engineering for Gas, Turbines and Power*, Vol.130, No.1, (January 2008), ISSN 0742-4795

Yang B.D.; Chu M.L. & Menq C.H. (1998). Stick–Slip–Separation Analysis and Non-Linear Stiffness and Damping Characterization of Friction Contacts Having Variable Normal Load, *Journal of Sound and Vibrations*, Vol.210, No.4, (March 1998), pp.461-481, ISSN 0022-460X

Yang B.D. & Menq C.H. (1998a). Characterization of Contact Kinematics and Application to the design of Wedge Dampers in Turbomachinery Blading: part 1 - Stick-slip Contact Kinematics, *ASME Journal of Engineering for Gas Turbine and Power*, Vol.120, No.2, (April 1998), pp.410-417, ISSN 0742-4795

Yang B.D. & Menq C.H. (1998b). Characterization of Contact Kinematics and Application to the design of Wedge Dampers in Turbomachinery Blading: part 2 - Prediction of Forced Response and Experimental Verification, *ASME Journal of Engineering for Gas Turbine and Power*, Vol.120, No.2, (April 1998), pp.418-423, ISSN 0742-4795

Yang B.D. & Menq C.H. (1998c). Characterization of 3D contact kinematics and prediction of resonant response of structures having 3D frictional constraint, *Journal of Sound and Vibration*, Vol.217, No.5, (November 1998), pp.909-925, ISSN 0022-460X

Zucca S.; Botto D. & Gola M.M. (2008). Range of Variability in the Dynamics of Semi-cylindrical friction dampers for turbine blades, (GT2008-51058), *Proceedings of ASME Turbo Expo*, ISBN 978-0-7918-4315-4, Berlin, Germany, June, 2008